AIMS Mathematics, 11(8): 25924–25957.
DOI: 10.3934/math.20261039
Received: 27 June 2026
Revised: 04 August 2026
Accepted: 07 August 2026
Published: 20 August 2026

https://www.aimspress.com/journal/Math

Research article

Structural feature amplification in malaria cell images via Hankel determinants and sine-associated Sakaguchi functions

Kamali R and S. Prema*

Department of Mathematics, SRM Institute of Science and Technology, Ramapuram, Chennai, Tamil Nadu, India

* **Correspondence:** Email: premnehaa@gmail.com; Tel: +919840483450.

Abstract: Logarithmic coefficients occupy an essential place in geometric function theory and are linked to univalent and close-to-convex functions. In this paper, the authors considered the third Hankel determinant connected with logarithmic coefficients of certain subfamilies of Sakaguchi functions, which also include sine-associated Sakaguchi functions. Sharp coefficient estimates and upper bounds were obtained for subclasses of functions, which led to obtaining new coefficient results in complex analysis and establishing connections between logarithmic coefficients and geometric function subclasses. Moreover, the proposed theoretical approach was used for enhancing the images of malaria cells with the help of the suggested Hankel-determinant-based image enhancement pipeline. Pixel intensity local distributions were considered via analytic functions, and logarithmic coefficients were used for computing the clarity factor required for adaptive sharpening of the image. Thus, a mathematically motivated Hankel-determinant-based image enhancement framework was developed, where a clipped clarity factor ensures stable enhancement. Experimental results demonstrated competitive image quality (PSNR = 23.92 dB, SSIM = 0.92, SNR = 18.66 dB, and CNR = 2.67) with improved preservation of chromatin structures and vacuoles, making the method suitable for malaria image preprocessing.

Keywords: holomorphic functions; Hankel determinant; subordination; logarithmic coefficients; Sakaguchi functions; malaria parasite detection; image enhancement
Mathematics Subject Classification: 30C45, 30C50

1. Introduction

Let $\mathbb{A}$ be the holomorphic function class within the open unit disk

$$\mathbf{U} = \{\zeta \in \mathbb{C} : |\zeta| < 1\},$$

which fulfills the requisite normalization criteria (see [1–3]), $f(0) = 0$ and $f'(0) = 1$. Consequently, every function $f \in \mathbb{A}$ may be expressed as a power series expansion of the form:

$$f(\zeta) = \zeta + \sum_{n=2}^{\infty} l_n \zeta^n, \quad \zeta \in \mathbf{U}. \tag{1}$$

Let $\mathbb{A}$ have a subclass $\mathcal{S}$ including one-one (injective) functions within $\mathbf{U}$ [4].

For two functions $h_1, h_2 \in \mathbb{A}$, we define h_1 as subordinate to h_2, explored in depth by Duren (2006) [5], denoted as $h_1 \prec h_2$, if ω exists satisfying the conditions [6]

$$|\omega(\zeta)| \leq |\zeta|, \qquad \omega(0) = 0,$$

and

$$h_1(\zeta) = h_2(\omega(\zeta)) \quad \text{for all } \zeta \in \mathbf{U}.$$

Raza et al. [7] explored subordination techniques (see Zeyani and Hussen, 2025) [8]. If $h_2 \in \mathcal{S}$, then it can be written as:

$$h_1 \prec h_2 \Leftrightarrow h_1(0) = h_2(0) \text{ and } h_1(\mathbf{U}) \subset h_2(\mathbf{U}).$$

The Ma-Minda class $\mathcal{S}^*(\Upsilon)$, introduced by Ma and Minda in 1992 [1,9], we introduce the following subclass associated with the sine function.

The principal objective of this paper is the sine-associated Sakaguchi-type class $\mathcal{S}^*_{\sin}$, which consists of normalized analytic functions satisfying the following subordination condition:

$$\mathcal{S}^*(\Upsilon) = \left\{ f \in \mathbb{A} : \frac{\zeta^{1-\mathcal{T}} f'(\zeta)}{[f(\zeta)]^{1-\mathcal{T}}} \prec \Upsilon(\zeta) \right\}, \tag{2}$$

where the choice of holomorphic function Υ determines the image $\Upsilon(\mathbf{U})$ of $\mathbf{U}$.

$$\Upsilon(0) = 1 \quad \text{and} \quad \Upsilon'(0) > 0.$$

Additionally, they looked into several practical geometric properties like covering results, expansion, and distortion. By choosing

$$\Upsilon(\zeta) = (1 + \zeta)(1 - \zeta)^{-1},$$

the class $\mathcal{S}^*(\Upsilon)$ reduces to the classical class of starlike functions. For different choices of the superordinate function Υ, the class $\mathcal{S}^*(\Upsilon)$ reduces to various well-known subclasses of starlike functions having distinct geometric properties [1].

Several choices of the Ma-Minda superordinate function have been investigated in the literature, including those associated with Fibonacci functions, conic regions, Bell numbers [10], spiral domains, and sigmoid mappings [11–13]. These studies have led to numerous subclasses of Ma-Minda starlike functions with diverse geometric properties. Pommerenke [14, 15] introduced $H_{b,n}(f)$ for $f \in \mathbb{A}$ as in (1).

Here, $H_{b,n}(f)$ [16, 17] is as follows:

$$H_{b,n}(f) = \begin{vmatrix} l_n & l_{n+1} & \cdots & l_{n+b-1} \\ l_{n+1} & l_{n+2} & \cdots & l_{n+b} \\ \vdots & \vdots & \ddots & \vdots \\ l_{n+b-1} & l_{n+b} & \cdots & l_{n+2b-2} \end{vmatrix}. \tag{3}$$

$H_{b,n}(f)$ for distinct orders is calculated for b and n of different values. If $n = 1$ and $b = 2$, the bound is as follows [18, 19]:

$$\left|H_{2,1}(f)\right| = \begin{vmatrix} l_1 & l_2 \\ l_2 & l_3 \end{vmatrix} = \left|l_3 - l_2^2\right|, \quad \text{where } l_1 = 1.$$

To get the second Hankel determinant, we set $b = n = 2$.

$$H_{2,2}(f) = \begin{vmatrix} l_2 & l_3 \\ l_3 & l_4 \end{vmatrix} = l_2 l_4 - l_3^2.$$

The Fekete-Szegö functional and Hankel determinants have been extensively investigated in the theory of univalent functions because of their importance in coefficient problems [20–22].

Khan et al. [19] established sharp bounds for several coefficient functionals associated with the class of bounded turning functions. Motivated by the study of Ma–Minda subclasses, Cho et al. [23] introduced the sine-associated starlike class defined by

$$\mathcal{S}^*_{\sin} = \left\{ f \in \mathcal{S} : \frac{\zeta^{1-\mathcal{T}} f'(\zeta)}{[f(\zeta)]^{1-\mathcal{T}}} \prec 1 + \sin(\zeta) \right\} \quad (\zeta \in D). \tag{4}$$

The choice of the superordinate function $1 + \sin\zeta$ is of particular interest because it generates a non-classical image domain with geometric properties that differ significantly from those of the classical starlike functions [24–26]. Consequently, many coefficient estimates available for the standard Ma-Minda subclasses cannot be transferred directly to this setting [27–29]. This motivates the study of logarithmic coefficients and Hankel determinant functionals for the generalized sine-associated Sakaguchi class. Although the sine-associated Ma-Minda class has been introduced previously, the corresponding generalized Sakaguchi-type class with parameter $\mathcal{T}$ has not been investigated from the viewpoint of logarithmic coefficient functionals and their associated Hankel determinants [30–32]. The introduction of the additional parameter $\mathcal{T}$ considerably enlarges the family under consideration and requires a separate coefficient analysis [33].

The logarithmic coefficients of, for $f \in \mathcal{S}$, $\mu_n = \mu_n(f)$ are given as [34–36]:

$$\log\left(\frac{f(\zeta)}{\zeta}\right) = 2\sum_{n=1}^{\infty} \mu_n \zeta^n.$$

Logarithmic coefficients play a crucial role in the work in [37–39]. The logarithmic coefficients for f provided by (1) are:

$$\mu_1 = \frac{1}{2} l_2, \tag{5}$$

$$\mu_2 = \frac{1}{2}\left(l_3 - \frac{1}{2} l_2^2\right), \tag{6}$$

$$\mu_3 = \frac{1}{2}\left(l_4 - l_2 l_3 + \frac{1}{3} l_2^2\right), \tag{7}$$

$$\mu_4 = \frac{1}{2}\left(l_5 - l_2 l_4 + l_2^2 l_3 - \frac{1}{2} l_3^2 - \frac{1}{4} l_2^4\right). \tag{8}$$

Following Khan et al. [1], we consider the Hankel determinant whose entries are the logarithmic coefficients of $f \in \mathcal{S}$, namely,

$$H_{b,n}(f) = \begin{vmatrix} \mu_n & \mu_{n+1} & \cdots & \mu_{n+b-1} \\ \mu_{n+1} & \mu_{n+2} & \cdots & \mu_{n+b} \\ \vdots & \vdots & \ddots & \vdots \\ \mu_{n+b-1} & \mu_{n+b} & \cdots & \mu_{n+2b-2} \end{vmatrix}. \tag{9}$$

The primary objective of this paper is to investigate the logarithmic coefficient problem for the generalized sine-associated Sakaguchi class $\mathcal{S}^*_{\sin}$. Unlike the previously studied sine-associated Ma-Minda class, the presence of the parameter leads to a more general family of analytic functions and introduces additional complexity into the coefficient relations. This paper establishes sharp bounds for the first four logarithmic coefficients together with the associated second-and third-order Hankel determinant functionals for this generalized class.

Motivated by this gap, we derive sharp upper bounds for the logarithmic coefficients μ_1, μ_2, μ_3, and μ_4, together with the functionals $\mu_1\mu_3 - \mu_2^2$, $\mu_2\mu_4 - \mu_3^2$, and $\mu_1\mu_4 - \mu_2\mu_3$. These estimates subsequently yield bounds for the corresponding Hankel determinant functionals associated with the logarithmic coefficients.

Furthermore, the theoretical results obtained in this work provide the mathematical foundation for the proposed Hankel-determinant-based image enhancement framework for malaria parasite cell visualization. Since the enhancement strategy is derived from the same Hankel determinant structure analysed in the mathematical part, the biomedical application serves as a direct consequence of the developed theory rather than as an independent image-processing study. The proposed enhancement method is further compared with classical edge detectors (Sobel, Canny, and Laplacian) as well as state-of-the-art enhancement techniques, including contrast limited adaptive histogram equalization (CLAHE), unsharp masking, single scale retinex (SSR), bilateral filtering, and non-local means (NLM), thereby demonstrating its effectiveness in preserving structural details and improving visualization quality.

The main contributions of this paper are summarized as follows:

- We investigate the generalized sine-associated Sakaguchi class $\mathcal{S}^*_{\sin}$, extending the previously studied sine-associated Ma-Minda class.
- We derive sharp estimates for the first four logarithmic coefficients of functions belonging to this class.
- We establish bounds for the associated second- and third-order Hankel determinant functionals.
- We demonstrate the applicability of the obtained theoretical results by constructing a Hankel-determinant-based framework for biomedical image enhancement and validating it on malaria parasite cell images.

2. A set of lemmas

$\mathcal{J}$ denotes the set of holomorphic functions j whose values are standardized by [2].

$$j(0) = 1 \quad \text{with} \quad \Re(j(\zeta)) > 0 \quad (\zeta \in \mathbf{U})$$

and are given by:

$$j(\zeta) = 1 + \sum_{n=1}^{\infty} c_n \zeta^n \quad (\zeta \in \mathbf{U}). \tag{10}$$

The given lemmas are used in our main results.

Lemma 2.1 ([40]). *For every $j \in \mathcal{J}$, one can find complex values x, δ with moduli not exceeding 1, i.e., $|x| \leq 1, |\delta| \leq 1$ such that*

$$2c_2 = c_1^2 + x(4 - c_1^2); \tag{11}$$

$$4c_3 = c_1^3 + 2(4 - c_1^2)c_1 x - c_1(4 - c_1^2)x^2 + 2(4 - c_1^2)(1 - |x|^2)\delta. \tag{12}$$

Lemma 2.2 ([1]). *Let*

$$j(\zeta) = 1 + \sum_{n=1}^{\infty} c_n \zeta^n \in \mathcal{J}.$$

Then the coefficients c_n satisfy the following inequalities:

$$|c_e| \leq 2 \text{ for } e \geq 1, \tag{13}$$

$$|c_{n+e} - \psi c_n c_e| < 2 \text{ for } 0 \leq \psi \leq 1, \tag{14}$$

$$|c_m c_e - c_e c_1| \leq 4 \text{ for } m + e = e + l, \quad \text{where } m, e, l \in \mathbb{N}, \tag{15}$$

$$|c_{e+2e} - \psi c_e c_e^2| \leq 2(1 + 2\psi), \quad \text{for } \psi \in \mathbb{R}, \tag{16}$$

$$\left| c_2 - \frac{c_1^2}{2} \right| \leq 2 - \frac{|c_1^2|}{2}, \tag{17}$$

and for ξ, we have

$$\left| c_2 - \xi c_1^2 \right| < 2 \max\{1, |2\xi - 1|\}, \quad \text{where } \xi \in \mathbb{R}. \tag{18}$$

For (13)–(17), see [15], and (18) is given in [21].

Lemma 2.3. *If $j \in \mathcal{J}$, then*

$$\left| \mathcal{I} c_1^3 - \mathcal{X} c_1 c_2 + \mathcal{V} c_3 \right| \leq 2|\mathcal{I}| + 2|\mathcal{X} - 2\mathcal{I}| + 2|\mathcal{I} - \mathcal{X} + \mathcal{V}|, \tag{19}$$

where $\mathcal{I}, \mathcal{X}$, and $\mathcal{V}$ are real-valued quantities (Khan et al., 2022 [1]) .

Notation. Throughout this paper, let

$$\mathbb{U} = \{ \zeta \in \mathbb{C} : |\zeta| < 1 \}$$

denote the open unit disk. The class $\mathcal{A}$ consists of functions of the form

$$f(\zeta) = \zeta + \sum_{n=2}^{\infty} l_n \zeta^n,$$

which are analytic in $\mathbb{U}$ and satisfy the normalization

$$f(0) = 0, \qquad f'(0) = 1.$$

The logarithmic coefficients are defined by

$$\log\left(\frac{f(\zeta)}{\zeta}\right) = 2\sum_{n=1}^{\infty}\mu_n\zeta^n.$$

Throughout this paper, the parameter $\mathcal{T}$ satisfies

$$0 \leq \mathcal{T} < 1.$$

For convenience, the notation and symbols used throughout the manuscript are summarized in Table 1.

Table 1. Notation used throughout the manuscript.

Symbol	Meaning
$\mathbb{U}$	Open unit disk
$\mathcal{A}$	Class of normalized analytic functions
l_n	Taylor coefficients of f
μ_n	Logarithmic coefficients
$\mathcal{T}$	Sakaguchi-type parameter ($0 \leq \mathcal{T} < 1$)
$H_{2,1}$, $H_{3,1}$	Hankel determinants
$\mathcal{S}^*_{\text{sin}}$	Sine-associated Sakaguchi class

Auxiliary notation. To simplify the lengthy algebraic expressions appearing in the proofs of the main results, we introduce the following abbreviations:

$$\begin{aligned} &\tau = \mathcal{T}, && \varrho_1 = \mathcal{T}+1, && F_2 = \mathcal{T}+2, && \vartheta_3 = \mathcal{T}+3,\\ &\kappa_4 = \mathcal{T}+4, && \varpi_1^* = \mathcal{T}-1, && \sigma_1^* = \mathcal{T}-2, && \phi_1^* = \mathcal{T}-3. \end{aligned}$$

These abbreviations are introduced solely to simplify lengthy algebraic expressions and have no independent mathematical significance.

3. Main results

Theorem 3.1. *If $f \in \mathcal{S}^*_{sin}$ and is written as in (1), then*

$$|\mu_1| \leq \frac{1}{2\varrho_1}, \tag{20}$$

$$|\mu_2| \leq \frac{1}{2F_2}, \tag{21}$$

$$|\mu_3| \leq \frac{1}{2\vartheta_3} + \frac{\varpi_1^*}{\varrho_1 F_2}\left(\frac{1}{2} + \frac{\varpi_1^* F_2}{4\varrho_1^2}\right), \tag{22}$$

$$|\mu_4| \leq \frac{1}{2\kappa_4} - \frac{1}{\kappa_4}\frac{(\varpi_1^*)^2\kappa_4}{\varrho_1^2 F_2}\left(\frac{1}{2} + \frac{\varpi_1^* F_2}{4\varrho_1^2}\right) - \frac{\varpi_1^*}{\varrho_1^2 F_2}\left(\frac{1}{2} + \frac{\varpi_1^* F_2}{4\varrho_1^2}\right). \tag{23}$$

Sharpness. For the special case $\mathcal{T} = 0$, the extremal functions listed below belong to the considered function class and attain equality in the corresponding logarithmic coefficient estimates. Therefore, the bounds established in Theorem 1 are sharp for $\mathcal{T} = 0$.

$$f_1(\zeta) = \zeta \exp\left(\int_0^\zeta \frac{\sin(t)}{t}\, dt\right) = \zeta + \zeta^2 + \cdots, \tag{24}$$

$$f_2(\zeta) = \zeta \exp\left(\int_0^\zeta \frac{\sin(t^2)}{t}\, dt\right) = \zeta + \frac{1}{2}\zeta^3 + \cdots, \tag{25}$$

$$f_3(\zeta) = \zeta \exp\left(\int_0^\zeta \frac{\sin(t^3)}{t}\, dt\right) = \zeta + \frac{1}{3}\zeta^4 + \cdots, \tag{26}$$

$$f_4(\zeta) = \zeta \exp\left(\int_0^\zeta \frac{\sin(t^4)}{t}\, dt\right) = \zeta + \frac{1}{4}\zeta^5 + \cdots. \tag{27}$$

Proof. Let $f \in \mathcal{S}^*_{\sin}$ with $\omega(0) = 0$ and $\omega(\zeta) < 1$, and then

$$\frac{\zeta^{1-\mathcal{T}} f'(\zeta)}{[f(\zeta)]^{1-\mathcal{T}}} = 1 + \sin(\omega(\zeta)). \tag{28}$$

The function is defined as [19]

$$p(\zeta) = \frac{1+\omega(\zeta)}{1-\omega(\zeta)} = 1 + c_1\zeta + c_2\zeta^2 + c_3\zeta^3 + \cdots.$$

Clearly, $p(\zeta) \in \mathcal{J}$, which leads to

$$\begin{aligned}\omega(\zeta) &= \frac{p(\zeta)-1}{p(\zeta)+1} = \frac{c_1\zeta + c_2\zeta^2 + c_3\zeta^3 + \cdots}{2 + c_1\zeta + c_2\zeta^2 + c_3\zeta^3 + \cdots} \\ &= \frac{1}{2}c_1\zeta + \left(\frac{1}{2}c_2 - \frac{1}{4}c_1^2\right)\zeta^2 + \left(\frac{1}{8}c_1^3 - \frac{1}{2}c_1c_2 + \frac{1}{2}c_3\right)\zeta^3 + \cdots.\end{aligned}$$

Now, from (28), we have

$$\begin{aligned}\frac{\zeta^{1-\mathcal{T}} f'(\zeta)}{[f(\zeta)]^{1-\mathcal{T}}} &= (\mathcal{T}+1)l_2\zeta + (\mathcal{T}+2)\left[l_3 + \frac{\mathcal{T}-1}{2}l_2^2\right]\zeta^2 \\ &\quad + (\mathcal{T}+3)\left[l_4 + (\mathcal{T}-1)l_2l_3 + \frac{(\mathcal{T}-1)(\mathcal{T}-2)}{6}l_2^3\right]\zeta^3 \\ &\quad + (\mathcal{T}+4)\Bigg[l_5 + (\mathcal{T}-1)\left(l_2l_4 + \frac{1}{2}l_3^2\right) \\ &\qquad + \frac{(\mathcal{T}-1)(\mathcal{T}-2)}{2}l_2^2l_3 + \frac{(\mathcal{T}-1)(\mathcal{T}-2)(\mathcal{T}-3)}{24}l_2^4\Bigg]\zeta^4 + \cdots\end{aligned} \tag{29}$$

and

$$\begin{aligned}1 + \sin(\omega(\zeta)) &= 1 + \frac{1}{2}c_1\zeta + \left(\frac{1}{2}c_2 - \frac{1}{4}c_1^2\right)\zeta^2 + \left(\frac{5}{48}c_1^3 - \frac{1}{2}c_1c_2 + \frac{1}{2}c_3\right)\zeta^3 \\ &\quad + \left(\frac{1}{2}c_4 - \frac{1}{2}c_1c_3 + \frac{5}{16}c_1^2c_2 - \frac{1}{4}c_2^2 - \frac{c_1^4}{32}\right)\zeta^4 + \cdots.\end{aligned} \tag{30}$$

Comparing (29) and (30), and applying the auxiliary notation defined above, we obtain

$$l_2 = \frac{c_1}{2\varrho_1}, \tag{31}$$

$$l_3 = \frac{1}{F_2}\left[\frac{1}{2}c_2 - \left(\frac{1}{4} + \frac{\varpi_1^* F_2}{8\varrho_1^2}\right)c_1^2\right], \tag{32}$$

$$l_4 = \frac{1}{\vartheta_3}\left[\frac{5 - \varpi_1^*\sigma_1^*\vartheta_3}{48\varrho_1^3}c_1^3 - \frac{1}{2}\left(1 + \frac{\vartheta_3\varpi_1^*}{2\varrho_1 F_2}\right)c_1c_2 + \frac{1}{2}c_3 + \frac{\vartheta_3\varpi_1^*}{4\varrho_1 F_2}\left(\frac{1}{2} + \frac{\varpi_1^* F_2}{4\varrho_1^2}\right)c_1^2\right], \tag{33}$$

$$\begin{aligned} l_5 = \frac{1}{\varkappa_4}\Bigg\{ & \frac{1}{2}c_4 + \left(-\frac{1}{2} - \frac{\varpi_1^*\varkappa_4}{4\varrho_1\vartheta_3}\right)c_1c_3 \\ & + \left[\frac{5}{16} + \frac{\varpi_1^*\varkappa_4}{4\varrho_1\vartheta_3}\left(1 + \frac{\vartheta_3\varpi_1^*}{2\varrho_1 F_2}\right) + \frac{\varpi_1^*\varkappa_4}{2F_2^2}\left(\frac{1}{4} + \frac{\varpi_1^* F_2}{8\varrho_1^2}\right) - \frac{\varpi_1^*\sigma_1^*\varkappa_4}{16\varrho_1^2 F_2}\right]c_1^2c_2 + \left(-\frac{1}{4} - \frac{\varpi_1^*\varkappa_4}{8F_2^2}\right)c_2^2 \\ & + \Bigg[-\frac{1}{32} - \frac{\varpi_1^*\varkappa_4}{2\varrho_1\vartheta_3}\cdot\frac{5 - \varpi_1^*\sigma_1^*\vartheta_3}{48\varrho_1^3} \\ & \quad - \frac{\varpi_1^*\varkappa_4}{2F_2^2}\left(\frac{1}{4} + \frac{\varpi_1^* F_2}{8\varrho_1^2}\right)^2 + \frac{\varpi_1^*\sigma_1^*\varkappa_4}{8\varrho_1^2 F_2}\left(\frac{1}{4} + \frac{\varpi_1^* F_2}{8\varrho_1^2}\right) - \frac{\varpi_1^*\sigma_1^*\phi_3^*\varkappa_4}{384\varrho_1^4}\Bigg]c_1^4 \\ & - \frac{(\varpi_1^*)^2\varkappa_4}{8\varrho_1^2 F_2}\left(\frac{1}{2} + \frac{\varpi_1^* F_2}{4\varrho_1^2}\right)c_1^3\Bigg\}. \end{aligned} \tag{34}$$

Now, from (5)–(8) and (31)–(34), we obtain

$$\mu_1 = \frac{1}{4\varrho_1}c_1, \tag{35}$$

$$\mu_2 = \frac{1}{2}\left\{\frac{1}{F_2}\left[\frac{1}{2}c_2 - \left(\frac{1}{4} + \frac{\varpi_1^* F_2}{8\varrho_1^2}\right)c_1^2\right] - \frac{1}{8\varrho_1^2}c_1^2\right\}, \tag{36}$$

$$\begin{aligned} \mu_3 = \frac{1}{2}\Bigg\{ & \left[\frac{5 - \varpi_1^*\sigma_1^*\vartheta_3 + 2\vartheta_3}{48\varrho_1^3\vartheta_3} + \frac{1}{2\varrho_1 F_2}\left(\frac{1}{4} + \frac{\varpi_1^* F_2}{8\varrho_1^2}\right)\right]c_1^3 \\ & - \left(\frac{1}{2\vartheta_3} + \frac{\tau}{4\varrho_1 F_2}\right)c_1c_2 + \frac{1}{2\vartheta_3}c_3 + \frac{\varpi_1^*}{4\varrho_1 F_2}\left(\frac{1}{2} + \frac{\varpi_1^* F_2}{4\varrho_1^2}\right)c_1^2\Bigg\}, \end{aligned} \tag{37}$$

$$\begin{aligned} \mu_4 = \frac{1}{2}\Bigg\{ & \frac{1}{2\varkappa_4}c_4 + \left[-\frac{1}{\varkappa_4}\left(\frac{1}{2} + \frac{\varpi_1^*\varkappa_4}{4\varrho_1\vartheta_3}\right) - \frac{1}{4\varrho_1\vartheta_3}\right]c_1c_3 \\ & + \Bigg[\frac{1}{\varkappa_4}\left(\frac{5}{16} + \frac{\varpi_1^*\varkappa_4}{4\varrho_1\vartheta_3}\left(1 + \frac{\vartheta_3\varpi_1^*}{2\varrho_1 F_2}\right) + \frac{\varpi_1^*\varkappa_4}{2F_2^2}\left(\frac{1}{4} + \frac{\varpi_1^* F_2}{8\varrho_1^2}\right) - \frac{\varpi_1^*\sigma_1^*\varkappa_4}{16\varrho_1^2 F_2}\right) \\ & \quad + \frac{1}{4\varrho_1\vartheta_3}\left(1 + \frac{\vartheta_3\varpi_1^*}{2\varrho_1 F_2}\right) + \frac{1}{8\varrho_1^2 F_2} + \frac{1}{2F_2^2}\left(\frac{1}{4} + \frac{\varpi_1^* F_2}{8\varrho_1^2}\right)\Bigg]c_1^2c_2 \\ & + \left[\frac{1}{\varkappa_4}\left(-\frac{1}{4} - \frac{\varpi_1^*\varkappa_4}{8F_2^2}\right) - \frac{1}{8F_2^2}\right]c_2^2 \\ & + \Bigg[\frac{1}{\varkappa_4}\Bigg(-\frac{1}{32} - \frac{\varpi_1^*\varkappa_4}{2\varrho_1\vartheta_3}\cdot\frac{5 - \varpi_1^*\sigma_1^*\vartheta_3}{48\varrho_1^3} - \frac{\varpi_1^*\varkappa_4}{2F_2^2}\left(\frac{1}{4} + \frac{\varpi_1^* F_2}{8\varrho_1^2}\right)^2 \end{aligned}$$

$$+\frac{\varpi_1^*\sigma_1^*\varkappa_4}{8\varrho_1^2F_2}\left(\frac{1}{4}+\frac{\varpi_1^*F_2}{8\varrho_1^2}\right)-\frac{\varpi_1^*\sigma_1^*\phi_3^*\varkappa_4}{24\cdot 16\varrho_1^4}\Bigg)$$
$$-\frac{1}{2\varrho_1\vartheta_3}\cdot\frac{5-\varpi_1^*\sigma_1^*\vartheta_3}{48\varrho_1^3}-\frac{1}{4\varrho_1^2F_2}\left(\frac{1}{4}+\frac{\varpi_1^*F_2}{8\varrho_1^2}\right)$$
$$-\frac{1}{2F_2^2}\left(\frac{1}{4}+\frac{\varpi_1^*F_2}{8\varrho_1^2}\right)^2-\frac{1}{64\varrho_1^4}\Bigg]c_1^4$$
$$+\left[-\frac{1}{\varkappa_4}\cdot\frac{(\varpi_1^*)^2\varkappa_4}{8\varrho_1^2F_2}\left(\frac{1}{2}+\frac{\varpi_1^*F_2}{4\varrho_1^2}\right)-\frac{\varpi_1^*}{8\varrho_1^2F_2}\left(\frac{1}{2}+\frac{\varpi_1^*F_2}{4\varrho_1^2}\right)\right]c_1^3\Bigg\}. \tag{38}$$

Applying (13) to (35), we get

$$|\mu_1|\le\frac{1}{2\varrho_1}.$$

From (36), using (17), we have

$$|\mu_2|=\frac{1}{4F_2}\left|c_2-\frac{1}{2}\left(1+\frac{\varpi_1^*F_2}{2\varrho_1^2}+\frac{F_2}{2\varrho_1^2}\right)c_1^2\right|\le\frac{1}{4F_2}\left(2-\left(1+\frac{\varpi_1^*F_2}{2\varrho_1^2}+\frac{F_2}{2\varrho_1^2}\right)\frac{|c_1|^2}{2}\right)=H(c_1).$$

Since $H(c_1)$ is a reducing function, reaching its maximum at $c_1=0$, then

$$|\mu_2|\le\frac{1}{2F_2}.$$

Applying (13) and Lemma 2.3 on Eq (37), we get

$$|\mu_3|\le\frac{1}{2\vartheta_3}+\frac{\varpi_1^*}{\varrho_1F_2}\left(\frac{1}{2}+\frac{\varpi_1^*F_2}{4\varrho_1^2}\right).$$

Rearranging (38) and applying (13) and (14), along with the triangular inequality, we get

$$|\mu_4|\le\frac{1}{2\varkappa_4}-\frac{1}{\varkappa_4}\frac{(\varpi_1^*)^2\varkappa_4}{\varrho_1^2F_2}\left(\frac{1}{2}+\frac{\varpi_1^*F_2}{4\varrho_1^2}\right)-\frac{\varpi_1^*}{\varrho_1^2F_2}\left(\frac{1}{2}+\frac{\varpi_1^*F_2}{4\varrho_1^2}\right).$$

To verify that the bounds in (21)–(24) are sharp, we examine specific functions for which the logarithmic coefficients attain the extreme values:

$$\log\frac{f_1(\zeta)}{\zeta}=2\sum_{n=2}^{\infty}\mu(f_1)\zeta^n=\zeta-\frac{1}{18}\zeta^3+\cdots,$$
$$\log\frac{f_2(\zeta)}{\zeta}=2\sum_{n=2}^{\infty}\mu(f_2)\zeta^n=\frac{1}{2}\zeta^2+\cdots,$$
$$\log\frac{f_3(\zeta)}{\zeta}=2\sum_{n=2}^{\infty}\mu(f_3)\zeta^n=\frac{1}{3}\zeta^3+\cdots,$$
$$\log\frac{f_4(\zeta)}{\zeta}=2\sum_{n=2}^{\infty}\mu(f_4)\zeta^n=\frac{1}{4}\zeta^4+\cdots.$$

The above logarithmic coefficient expansions show that the corresponding coefficients attain the upper bounds. Hence, equality is attained for the special case where $\mathcal{T}=0$, establishing the sharpness of the bounds in Theorem 3.1 for $\mathcal{T}=0$. □

Theorem 3.2. *If $f \in \mathcal{S}^*_{\sin}$ and has the representation given in (1), then*

$$|\mu_1\mu_3 - \mu_2^2| \leq \frac{1}{4F_2^2}. \tag{39}$$

As shown in (25), the function f_2 demonstrates that the bound is sharp.

Proof. From (35)–(37), we obtain

$$\mu_1\mu_3 - \mu_2^2 = Ac_1^4 + Bc_1^2c_2 + Cc_1^3 + Dc_1c_3 + Ec_2^2 + Fc_1c_2,$$

where

$$\begin{aligned}
A &= \left\{\frac{1}{8\varrho_1}\left[\frac{5 - \varpi_1^*\sigma_1^*\vartheta_3 + 2\vartheta_3}{48\varrho_1^3\vartheta_3} + \frac{1}{2\varrho_1F_2}\left(\frac{1}{4} + \frac{\varpi_1^*F_2}{8\varrho_1^2}\right)\right]\right.\\
&\quad \left. - \frac{1}{4F_2^2}\left(\frac{1}{4} + \frac{\varpi_1^*F_2}{8\varrho_1^2}\right)^2 - \frac{1}{256\varrho_1^4} - \frac{1}{16\varrho_1^2F_2}\left(\frac{1}{4} + \frac{\varpi_1^*F_2}{8\varrho_1^2}\right)\right\},\\
B &= \left[-\frac{1}{8\varrho_1}\left(\frac{1}{2\vartheta_3} + \frac{\tau}{4\varrho_1F_2}\right) + \frac{1}{32\varrho_1^2F_2}\right],\\
C &= \frac{\varpi_1^*}{32\varrho_1^2F_2}\left(\frac{1}{2} + \frac{\varpi_1^*F_2}{4\varrho_1^2}\right),\\
D &= \frac{1}{16\varrho_1\vartheta_3},\\
E &= -\frac{1}{16F_2^2},\\
F &= \frac{1}{4F_2^2}\left(\frac{1}{4} + \frac{\varpi_1^*F_2}{8\varrho_1^2}\right).
\end{aligned}$$

Utilizing Lemma 2.1, we can represent c_2 and c_3 as functions of $c_1 = c \in [0, 2]$, and thus

$$\begin{aligned}
\mu_1\mu_3 - \mu_2^2 &= \left(A + \frac{B}{2} + \frac{D}{4} + \frac{E}{4}\right)c^4 + \left(\frac{B}{2} + \frac{D}{2}\right)xc^2(4 - c^2) + \left(C + \frac{F}{2}\right)c^3\\
&\quad - \frac{D}{4}c^2x^2(4 - c^2) + \frac{D}{2}c(4 - c^2)(1 - |x|^2)\delta\\
&\quad + \left(\frac{E}{2} + \frac{F}{2}\right)cx(4 - c^2) + \frac{E}{4}x^2(4 - c^2)^2.
\end{aligned}$$

Utilizing the triangle inequality, with $|\delta| \leq 1$ and $|x| = y \leq 1$, it follows that

$$\begin{aligned}
|\mu_1\mu_3 - \mu_2^2| &\leq \left(A + \frac{B}{2} + \frac{D}{4} + \frac{E}{4}\right)c^4 + \left(\frac{B}{2} + \frac{D}{2}\right)yc^2(4 - c^2) + \left(C + \frac{F}{2}\right)c^3\\
&\quad - \frac{D}{4}c^2y^2(4 - c^2) + \frac{D}{2}c(4 - c^2)(1 - y^2) + \left(\frac{E}{2} + \frac{F}{2}\right)cy(4 - c^2)\\
&\quad + \frac{E}{4}y^2(4 - c^2)^2 = G(c, y) \quad \text{(say)}.
\end{aligned}$$

Now, differentiating $G(c, y)$ partially with respect to y, we obtain

$$\frac{\partial G(c,y)}{\partial y} = \left(\frac{B}{2} + \frac{D}{2}\right)c^2(4-c^2) - \frac{2Dc^2}{4}y(4-c^2) - \frac{2Dc}{4}y(4-c^2) + \left(\frac{E}{2} + \frac{F}{2}\right)c(4-c^2) + \frac{Ey}{2}(4-c^2)^2.$$

Since

$$0 \le c \le 2, \qquad 0 \le y \le 1,$$

the above derivative is continuous on the admissible domain. Moreover, the coefficients appearing in the derivative satisfy the required sign conditions under the parameter restrictions of Theorem 3.2. Consequently,

$$\frac{\partial G(c,y)}{\partial y} > 0.$$

Hence, for each fixed c, the function $G(c, y)$ is increasing with respect to y, and therefore its maximum is attained at $y = 1$:

$$\begin{aligned} G(c,y) &\le G(c,1) \\ &= \left(A + \frac{B}{2} + \frac{D}{4} + \frac{E}{4}\right)c^4 + \left(\frac{B}{2} + \frac{D}{2}\right)c^2(4-c^2) + \left(C + \frac{F}{2}\right)c^3 \\ &\quad - \frac{D}{4}c^2(4-c^2) + \left(\frac{E}{2} + \frac{F}{2}\right)c(4-c^2) + \frac{E}{4}(4-c^2)^2 \\ &= \left(A + \frac{E}{2}\right)c^4 + (2B + D - 2E)c^2 + \left(C - \frac{E}{2}\right)c^3 + 2(E+F)c + 4E. \end{aligned}$$

Now, differentiating the expansion with respect to c, we have

$$G'(c,1) = \left(A + \frac{E}{2}\right)4c^3 + 2(2B + D - 2E)c + 3\left(C - \frac{E}{2}\right)c^2 + 2(E+F).$$

$$\begin{aligned} G'(c,1) = -\Bigg\{ &\frac{1}{8\varrho_1}\left[\frac{1}{4F_2^2}\left(\frac{1}{4} + \frac{\varpi_1^* F_2}{8\varrho_1^2}\right)^2 + \frac{1}{256\varrho_1^4} + \frac{1}{16\varrho_1^2 F_2}\left(\frac{1}{4} + \frac{\varpi_1^* F_2}{8\varrho_1^2}\right)\right. \\ &\left. + \frac{1}{32F_2^2} - \frac{5 - \varpi_1^*\sigma_1^*\vartheta_3 + 2\vartheta_3}{48\varrho_1^3\vartheta_3} - \frac{1}{2\varrho_1 F_2}\left(\frac{1}{4} + \frac{\varpi_1^* F_2}{8\varrho_1^2}\right)\right]\Bigg\}4c^3 \\ &- \left\{\frac{1}{2\varrho_1}\left(\frac{1}{2\vartheta_3} + \frac{\tau}{4\varrho_1 F_2} + \frac{1}{32\varrho_1^2 F_2} + \frac{1}{8F_2^2} - \frac{1}{16\varrho_1\vartheta_3}\right)\right\}c \\ &- \frac{3}{32F_2}\left[\frac{1}{F_2} - \frac{\varpi_1^*}{\varrho_1^2}\left(\frac{1}{2} + \frac{\varpi_1^* F_2}{4\varrho_1^2}\right)\right]c^2 - \frac{1}{4F_2^2}\left[\frac{1}{2} - \frac{1}{4} - \frac{\varpi_1^* F_2}{8\varrho_1^2}\right]. \end{aligned}$$

Since $0 \le c \le 2$, the polynomial $G'(c, 1)$ satisfies the required sign condition under the admissible parameter restrictions of Theorem 3.2. Therefore, $G'(c, 1) \le 0$.

Hence, $G(c, 1)$ is decreasing on the interval $[0, 2]$, and consequently, its maximum value is attained at $c = 0$:

$$|\mu_1\mu_3 - \mu_2^2| \le 4E = 4\left(\frac{1}{16F_2^2}\right),$$

and we have,

$$|\mu_1\mu_3 - \mu_2^2| \le \frac{1}{4F_2^2}.$$

□

Theorem 3.3. *Let $f \in \mathcal{S}^*_{sin}$ be given by the expansion in (1), and then*

$$\begin{aligned}
&\left|\mu_2\mu_4-\mu_3^2\right| \leq \left\{\frac{1}{8F_2}\left[\frac{1}{\varkappa_4}\left(\frac{1}{32}+\frac{\varpi_1^*\varkappa_4}{2\varrho_1\vartheta_3}\left(\frac{5-\varpi_1^*\sigma_1^*\vartheta_3}{48\varrho_1^3}\right)+\frac{\varpi_1^*\varkappa_4}{2F_2^2}\left(\frac{1}{4}+\frac{\varpi_1^*F_2}{8\varrho_1^2}\right)^2\right.\right.\right.\\
&-\frac{\varpi_1^*\sigma_1^*\varkappa_4}{8\varrho_1^2F_2}\left(\frac{1}{4}+\frac{\varpi_1^*F_2}{8\varrho_1^2}\right)+\frac{\varpi_1^*\sigma_1^*\phi_3^*\varkappa_4}{384\varrho_1^4}\Big)+\frac{1}{2\varrho_1\vartheta_3}\left(\frac{5-\varpi_1^*\sigma_1^*\vartheta_3}{48\varrho_1^3}\right)\\
&\left.+\frac{1}{4\varrho_1^2F_2}\left(\frac{1}{4}+\frac{\varpi_1^*F_2}{8\varrho_1^2}\right)+\frac{1}{2F_2^2}\left(\frac{1}{4}+\frac{\varpi_1^*F_2}{8\varrho_1^2}\right)^2+\frac{1}{64\varrho_1^4}\right]\\
&-\frac{1}{2}\left(\frac{1}{2F_2}\left(\frac{1}{4}+\frac{\varpi_1^*F_2}{8\varrho_1^2}\right)+\frac{1}{16\varrho_1^2}\right)\left[\frac{1}{\varkappa_4}\left(\frac{5}{16}+\frac{\varpi_1^*\varkappa_4}{4\varrho_1\vartheta_3}\left(1+\frac{\vartheta_3\varpi_1^*}{2\varrho_1F_2}\right)\right.\right.\\
&\left.\left.+\frac{\varpi_1^*\varkappa_4}{2F_2^2}\left(\frac{1}{4}+\frac{\varpi_1^*F_2}{8\varrho_1^2}\right)-\frac{\varpi_1^*\sigma_1^*\varkappa_4}{16\varrho_1^2F_2}\right)+\frac{1}{4\varrho_1\vartheta_3}\left(1+\frac{\vartheta_3\varpi_1^*}{2\varrho_1F_2}\right)+\frac{1}{8\varrho_1^2F_2}+\frac{1}{2F_2^2}\left(\frac{1}{4}+\frac{\varpi_1^*F_2}{8\varrho_1^2}\right)\right]\Bigg\}\times 2^5\\
&+\frac{2}{\varkappa_4}\left[\frac{1}{2F_2}\left(\frac{1}{4}+\frac{\varpi_1^*F_2}{8\varrho_1^2}\right)+\frac{1}{16\varrho_1^2}\right]+\frac{1}{4\varkappa_4F_2}\\
&+\left\{\frac{1}{2}\left[\frac{1}{2F_2}\left(\frac{1}{4}+\frac{\varpi_1^*F_2}{8\varrho_1^2}\right)+\frac{1}{16\varrho_1^2}\right]\left[\frac{1}{\varkappa_4}\left(\frac{1}{2}+\frac{\varpi_1^*\varkappa_4}{4\varrho_1\vartheta_3}\right)+\frac{1}{4\varrho_1\vartheta_3}\right]\right.\\
&\left.-\frac{1}{4}\left[\frac{5-\varpi_1^*\sigma_1^*\vartheta_3+2\vartheta_3}{48\varrho_1^3\vartheta_3}+\frac{1}{2\varrho_1F_2}\left(\frac{1}{4}+\frac{\varpi_1^*F_2}{8\varrho_1^2}\right)\right]\frac{1}{\vartheta_3}\right\}\times 2^4\\
&+\frac{1}{4\vartheta_3^2}+\frac{\varpi_1^*}{2\vartheta_3\varrho_1F_2}\left(\frac{1}{2}+\frac{\varpi_1^*F_2}{4\varrho_1^2}\right)+4\left[\frac{\varpi_1^*}{4\varrho_1F_2}\left(\frac{1}{2}+\frac{\varpi_1^*F_2}{4\varrho_1^2}\right)\right]^2\\
&+\left\{\frac{1}{2}\left[\frac{1}{2F_2}\left(\frac{1}{4}+\frac{\varpi_1^*F_2}{8\varrho_1^2}\right)+\frac{1}{16\varrho_1^2}\right]\left[\frac{(\varpi_1^*)^2}{8\varrho_1^2F_2}\left(\frac{1}{2}+\frac{\varpi_1^*F_2}{4\varrho_1^2}\right)+\frac{\varpi_1^*}{8\varrho_1^2F_2}\left(\frac{1}{2}+\frac{\varpi_1^*F_2}{4\varrho_1^2}\right)\right]\right.\\
&\left.-\frac{1}{2}\left[\frac{5-\varpi_1^*\sigma_1^*\vartheta_3+2\vartheta_3}{48\varrho_1^3\vartheta_3}+\frac{1}{2\varrho_1F_2}\left(\frac{1}{4}+\frac{\varpi_1^*F_2}{8\varrho_1^2}\right)\right]\frac{\varpi_1^*}{4\varrho_1F_2}\left(\frac{1}{2}+\frac{\varpi_1^*F_2}{4\varrho_1^2}\right)\right\}\times 2^5\\
&+\frac{1}{8F_2}\left[-\frac{(\varpi_1^*)^2}{8\varrho_1^2F_2}\left(\frac{1}{2}+\frac{\varpi_1^*F_2}{4\varrho_1^2}\right)-\frac{\varpi_1^*}{8\varrho_1^2F_2}\left(\frac{1}{2}+\frac{\varpi_1^*F_2}{4\varrho_1^2}\right)\right]\\
&+\frac{1}{2}\left(\frac{1}{2\vartheta_3}+\frac{\tau}{4\varrho_1F_2}\right)\frac{\varpi_1^*}{4\varrho_1F_2}\left(\frac{1}{2}+\frac{\varpi_1^*F_2}{4\varrho_1^2}\right)\Bigg\}\times 2^4. \qquad (40)
\end{aligned}$$

Proof. From (36)–(38), we get

$$\begin{aligned}
\mu_2\mu_4-\mu_3^2 = {} & Ac_1^6-Bc_1^4c_2+Cc_1^3c_3+Dc_1^2c_2^2-Ec_4c_1^2+Fc_1c_2c_3\\
& -Gc_2^3+Hc_4c_2-Ic_3^2-Jc_1^2c_3-Kc_1^4+Lc_1^5+Mc_1^3c_2,
\end{aligned}$$

where

$$\begin{aligned}
A = {} & \left\{-\frac{1}{2}\left[\frac{1}{2F_2}\left(\frac{1}{4}+\frac{\varpi_1^*F_2}{8\varrho_1^2}\right)+\frac{1}{16\varrho_1^2}\right]\times\left\{\frac{1}{\varkappa_4}\left[-\frac{1}{32}-\frac{\varpi_1^*\varkappa_4}{2\varrho_1\vartheta_3}\left(\frac{5-\varpi_1^*\sigma_1^*\vartheta_3}{48\varrho_1^3}\right)-\frac{\varpi_1^*\varkappa_4}{2F_2^2}\left(\frac{1}{4}+\frac{\varpi_1^*F_2}{8\varrho_1^2}\right)^2\right.\right.\right.\\
& \left.\left.+\frac{\varpi_1^*\sigma_1^*\varkappa_4}{8\varrho_1^2F_2}\left(\frac{1}{4}+\frac{\varpi_1^*F_2}{8\varrho_1^2}\right)-\frac{\varpi_1^*\sigma_1^*\phi_3^*\varkappa_4}{384\varrho_1^4}\right]-\frac{1}{2\varrho_1\vartheta_3}\left(\frac{5-\varpi_1^*\sigma_1^*\vartheta_3}{48\varrho_1^3}\right)-\frac{1}{4\varrho_1^2F_2}\left(\frac{1}{4}+\frac{\varpi_1^*F_2}{8\varrho_1^2}\right)
\end{aligned}$$

$$
\begin{aligned}
&- \frac{1}{2F_2^2}\left(\frac{1}{4}+\frac{\varpi_1^* F_2}{8\varrho_1^2}\right)^2 - \frac{1}{64\varrho_1^4}\Bigg\} - \frac{1}{4}\Bigg[\frac{5-\varpi_1^*\sigma_1^*\vartheta_3+2\vartheta_3}{48\varrho_1^3\vartheta_3}+\frac{1}{2\varrho_1 F_2}\left(\frac{1}{4}+\frac{\varpi_1^* F_2}{8\varrho_1^2}\right)\Bigg]^2\Bigg\},\\
B = &\Bigg\{\frac{1}{8F_2}\Bigg\{\frac{1}{\varkappa_4}\Bigg[\frac{1}{32}+\frac{\varpi_1^*\varkappa_4}{2\varrho_1\vartheta_3}\left(\frac{5-\varpi_1^*\sigma_1^*\vartheta_3}{48\varrho_1^3}\right)+\frac{\varpi_1^*\varkappa_4}{2F_2^2}\left(\frac{1}{4}+\frac{\varpi_1^* F_2}{8\varrho_1^2}\right)^2\\
&- \frac{\varpi_1^*\sigma_1^*\varkappa_4}{8\varrho_1^2 F_2}\left(\frac{1}{4}+\frac{\varpi_1^* F_2}{8\varrho_1^2}\right)+\frac{\varpi_1^*\sigma_1^*\phi_3^*\varkappa_4}{384\varrho_1^4}\Bigg]+\frac{1}{2\varrho_1\vartheta_3}\left(\frac{5-\varpi_1^*\sigma_1^*\vartheta_3}{48\varrho_1^3}\right)+\frac{1}{4\varrho_1^2 F_2}\left(\frac{1}{4}+\frac{\varpi_1^* F_2}{8\varrho_1^2}\right)\\
&+ \frac{1}{2F_2^2}\left(\frac{1}{4}+\frac{\varpi_1^* F_2}{8\varrho_1^2}\right)^2+\frac{1}{64\varrho_1^4}\Bigg\} - \frac{1}{2}\left(\frac{1}{2F_2}\left(\frac{1}{4}+\frac{\varpi_1^* F_2}{8\varrho_1^2}\right)+\frac{1}{16\varrho_1^2}\right)\\
&\times\Bigg\{\frac{1}{\varkappa_4}\Bigg[\frac{5}{16}+\frac{\varpi_1^*\varkappa_4}{4\varrho_1\vartheta_3}\left(1+\frac{\vartheta_3\varpi_1^*}{2\varrho_1 F_2}\right)+\frac{\varpi_1^*\varkappa_4}{2F_2^2}\left(\frac{1}{4}+\frac{\varpi_1^* F_2}{8\varrho_1^2}\right)-\frac{\varpi_1^*\sigma_1^*\varkappa_4}{16\varrho_1^2 F_2}\Bigg]\\
&+ \frac{1}{4\varrho_1\vartheta_3}\left(1+\frac{\vartheta_3\varpi_1^*}{2\varrho_1 F_2}\right)+\frac{1}{8\varrho_1^2 F_2}+\frac{1}{2F_2^2}\left(\frac{1}{4}+\frac{\varpi_1^* F_2}{8\varrho_1^2}\right)\Bigg\}\Bigg\},\\
C = &\Bigg\{\frac{1}{2}\left[\frac{1}{2F_2}\left(\frac{1}{4}+\frac{\varpi_1^* F_2}{8\varrho_1^2}\right)+\frac{1}{16\varrho_1^2}\right]\left[\frac{1}{\varkappa_4}\left(\frac{1}{2}+\frac{\varpi_1^*\varkappa_4}{4\varrho_1\vartheta_3}\right)+\frac{1}{4\varrho_1\vartheta_3}\right]\\
&- \frac{1}{4}\left[\frac{5-\varpi_1^*\sigma_1^*\vartheta_3+2\vartheta_3}{48\varrho_1^3\vartheta_3}+\frac{1}{2\varrho_1 F_2}\left(\frac{1}{4}+\frac{\varpi_1^* F_2}{8\varrho_1^2}\right)\right]\frac{1}{\vartheta_3}\Bigg\},\\
D = &\frac{1}{8F_2\varkappa_4}\left[\frac{5}{16}+\frac{\varpi_1^*\varkappa_4}{4\varrho_1\vartheta_3}\left(1+\frac{\vartheta_3\varpi_1^*}{2\varrho_1 F_2}\right)+\frac{\varpi_1^*\varkappa_4}{2F_2^2}\left(\frac{1}{4}+\frac{\varpi_1^* F_2}{8\varrho_1^2}\right)-\frac{\varpi_1^*\sigma_1^*\varkappa_4}{16\varrho_1^2 F_2}\right]\\
&+ \frac{1}{32\varrho_1 F_2\vartheta_3}\left(1+\frac{\vartheta_3\varpi_1^*}{2\varrho_1 F_2}\right)+\frac{1}{64\varrho_1^2 F_2^2}+\frac{1}{16F_2^3}\left(\frac{1}{4}+\frac{\varpi_1^* F_2}{8\varrho_1^2}\right)\\
&- \frac{1}{2}\left[\frac{1}{2F_2}\left(\frac{1}{4}+\frac{\varpi_1^* F_2}{8\varrho_1^2}\right)+\frac{1}{16\varrho_1^2}\right]\left[\frac{1}{\varkappa_4}\left(-\frac{1}{4}-\frac{\varpi_1^*\varkappa_4}{8F_2^2}\right)-\frac{1}{8F_2^2}\right]-\frac{1}{4}\left(\frac{1}{2\vartheta_3}+\frac{\tau}{4\varrho_1 F_2}\right)^2,\\
E = &\frac{1}{4\varkappa_4}\left[\frac{1}{2F_2}\left(\frac{1}{4}+\frac{\varpi_1^* F_2}{8\varrho_1^2}\right)+\frac{1}{16\varrho_1^2}\right],\\
F = &\Bigg\{\frac{1}{8F_2}\left[-\frac{1}{\varkappa_4}\left(\frac{1}{2}+\frac{\varpi_1^*\varkappa_4}{4\varrho_1\vartheta_3}\right)-\frac{1}{4\varrho_1\vartheta_3}\right]+\frac{1}{4}\left(\frac{1}{2\vartheta_3}+\frac{\tau}{4\varrho_1 F_2}\right)\frac{1}{\vartheta_3}\Bigg\},\\
G = &\frac{1}{8F_2}\left[\frac{1}{\varkappa_4}\left(\frac{1}{4}+\frac{\varpi_1^*\varkappa_4}{8F_2^2}\right)+\frac{1}{8F_2^2}\right],\\
H = &\frac{1}{16\varkappa_4 F_2},\\
I = &\frac{1}{16\vartheta_3^2},\\
J = &\frac{\varpi_1^*}{4\vartheta_3 4\varrho_1 F_2}\left(\frac{1}{2}+\frac{\varpi_1^* F_2}{4\varrho_1^2}\right),\\
K = &\frac{1}{4}\left[\frac{\varpi_1^*}{4\varrho_1 F_2}\left(\frac{1}{2}+\frac{\varpi_1^* F_2}{4\varrho_1^2}\right)\right]^2,
\end{aligned}
$$

$$L = \left\{\frac{1}{2}\left[\frac{1}{2F_2}\left(\frac{1}{4}+\frac{\varpi_1^* F_2}{8\varrho_1^2}\right)+\frac{1}{16\varrho_1^2}\right]\left[\frac{(\varpi_1^*)^2}{8\varrho_1^2 F_2}\left(\frac{1}{2}+\frac{\varpi_1^* F_2}{4\varrho_1^2}\right)+\frac{\varpi_1^*}{8\varrho_1^2 F_2}\left(\frac{1}{2}+\frac{\varpi_1^* F_2}{4\varrho_1^2}\right)\right]\right.$$
$$\left.-\frac{1}{2}\left[\frac{5-\varpi_1^*\sigma_1^*\vartheta_3+2\vartheta_3}{48\varrho_1^3\vartheta_3}+\frac{1}{2\varrho_1 F_2}\left(\frac{1}{4}+\frac{\varpi_1^* F_2}{8\varrho_1^2}\right)\right]\frac{\varpi_1^*}{4\varrho_1 F_2}\left(\frac{1}{2}+\frac{\varpi_1^* F_2}{4\varrho_1^2}\right)\right\},$$
$$M = \frac{1}{8F_2}\left[-\frac{(\varpi_1^*)^2}{8\varrho_1^2 F_2}\left(\frac{1}{2}+\frac{\varpi_1^* F_2}{4\varrho_1^2}\right)-\frac{\varpi_1^*}{8\varrho_1^2 F_2}\left(\frac{1}{2}+\frac{\varpi_1^* F_2}{4\varrho_1^2}\right)\right]+\frac{1}{2}\left(\frac{1}{2\vartheta_3}+\frac{\tau}{4\varrho_1 F_2}\right)\frac{\varpi_1^*}{4\varrho_1 F_2}\left(\frac{1}{2}+\frac{\varpi_1^* F_2}{4\varrho_1^2}\right).$$

Rearranging the above, we have

$$\left|\mu_2\mu_4-\mu_3^2\right| = \left|-Bc_1^4\left(c_2-\frac{A}{B}c_1^2\right)-Ec_1^2\left(c_4-\frac{D}{E}c_2^2\right)+Hc_2\left(c_4-\frac{G}{H}c_2^2\right)\right.$$
$$\left.+Cc_1^3c_3-Ic_3\left(c_3-\frac{F}{I}c_1c_2\right)-Jc_1^2c_3-Kc_1^4+Lc_1^5+Mc_1^3c_2\right|.$$

Applying the triangle inequality, we get

$$\left|\mu_2\mu_4-\mu_3^2\right| \le B\left|c_1\right|^4\left|c_2-\frac{A}{B}c_1^2\right|+E\left|c_1\right|^2\left|c_4-\frac{D}{E}c_2^2\right|$$
$$+H\left|c_2\right|\left|c_4-\frac{G}{H}c_2^2\right|+C\left|c_1\right|^3\left|c_3\right|$$
$$+I\left|c_3\right|\left|c_3-\frac{F}{I}c_1c_2\right|+J\left|c_1\right|^2\left|c_3\right|+K\left|c_1\right|^4$$
$$+L\left|c_1\right|^5+M\left|c_1\right|^3\left|c_2\right|.$$

Using (13) and (14), we get

$$\left|\mu_2\mu_4-\mu_3^2\right| \le B\cdot 2^5+E\cdot 2^3+H\cdot 2^2+C\cdot 2^4+I\cdot 2^2+J\cdot 2^3+K\cdot 2^4$$
$$+L\cdot 2^5+M\cdot 2^4.$$

Substituting the values of B, E, H, C, I, J, K, L, and M we get the required result. □

Theorem 3.4. *Let $f \in \mathcal{S}_{sin}^*$ and be given by (1). Then*

$$\left|\mu_1\mu_4-\mu_2\mu_3\right| \le 2^4\left\{\frac{1}{8\varrho_1\varkappa_4}\left[\frac{5}{16}+\frac{\varpi_1^*\varkappa_4}{4\varrho_1\vartheta_3}\left(1+\frac{\vartheta_3\varpi_1^*}{2\varrho_1 F_2}\right)+\frac{\varpi_1^*\varkappa_4}{2F_2^2}\left(\frac{1}{4}+\frac{\varpi_1^* F_2}{8\varrho_1^2}\right)-\frac{\varpi_1^*\sigma_1^*\varkappa_4}{16\varrho_1^2 F_2}\right]\right.$$
$$+\frac{1}{32\varrho_1^2\vartheta_3}\left(1+\frac{\varpi_1^*\vartheta_3}{2\varrho_1 F_2}\right)+\frac{1}{64\varrho_1^3 F_2}+\frac{1}{16\varrho_1 F_2^2}\left(\frac{1}{4}+\frac{\varpi_1^* F_2}{8\varrho_1^2}\right)$$
$$-\frac{1}{4F_2}\left[\frac{5-\varpi_1^*\sigma_1^*\vartheta_3+2\vartheta_3}{96\varrho_1^3\vartheta_3}+\frac{1}{4\varrho_1 F_2}\left(\frac{1}{4}+\frac{\varpi_1^* F_2}{8\varrho_1^2}\right)\right]$$
$$\left.-\frac{1}{2}\left(\frac{1}{2\vartheta_3}+\frac{\tau}{4\varrho_1 F_2}\right)\left[\frac{1}{2F_2}\left(\frac{1}{4}+\frac{\varpi_1^* F_2}{8\varrho_1^2}\right)+\frac{1}{16\varrho_1^2}\right]\right\}$$
$$+\frac{1}{4\varrho_1\varkappa_4}+\frac{1}{4F_2\vartheta_3}+\frac{\varpi_1^*}{4\varrho_1 F_2^2}\left(\frac{1}{2}+\frac{\varpi_1^* F_2}{4\varrho_1^2}\right). \tag{41}$$

Proof. From (35)–(38), we get

$$\mu_1\mu_4 - \mu_2\mu_3 = -Ac_1^5 + Bc_1^3c_2 - Cc_3c_1^2 + Dc_4c_1 + Ec_1c_2^2 - Fc_3c_2 + Gc_1^4 - Hc_1^2c_2,$$

where

$$\begin{aligned}
A = &\left\{\frac{1}{8\varrho_1\varkappa_4}\left[\frac{1}{32} + \frac{\varpi_1^*\varkappa_4}{2\varrho_1\vartheta_3}\left(\frac{5-\varpi_1^*\sigma_1^*\vartheta_3}{48\varrho_1^3}\right) + \frac{\varpi_1^*\varkappa_4}{2F_2^2}\left(\frac{1}{4}+\frac{\varpi_1^*F_2}{8\varrho_1^2}\right)^2 - \frac{\varpi_1^*\sigma_1^*\varkappa_4}{8\varrho_1^2F_2}\left(\frac{1}{4}+\frac{\varpi_1^*F_2}{8\varrho_1^2}\right) + \frac{\varpi_1^*\sigma_1^*\phi_3^*\varkappa_4}{384\varrho_1^4}\right]\right.\\
&+ \frac{1}{16\varrho_1^2\vartheta_3}\left(\frac{5-\varpi_1^*\sigma_1^*\vartheta_3}{48\varrho_1^3}\right) + \frac{1}{32\varrho_1^3F_2}\left(\frac{1}{4}+\frac{\varpi_1^*F_2}{8\varrho_1^2}\right) + \frac{1}{16\varrho_1F_2^2}\left(\frac{1}{4}+\frac{\varpi_1^*F_2}{8\varrho_1^2}\right)^2 + \frac{1}{512\varrho_1^4}\\
&\left.- \left[\frac{1}{2F_2}\left(\frac{1}{4}+\frac{\varpi_1^*F_2}{8\varrho_1^2}\right) + \frac{1}{16\varrho_1^2}\right]\left[\frac{5-\varpi_1^*\sigma_1^*\vartheta_3+2\vartheta_3}{96\varrho_1^3\vartheta_3} + \frac{1}{4\varrho_1F_2}\left(\frac{1}{4}+\frac{\varpi_1^*F_2}{8\varrho_1^2}\right)\right]\right\},\\
B = &\left\{\frac{1}{8\varrho_1\varkappa_4}\left[\frac{5}{16} + \frac{\varpi_1^*\varkappa_4}{4\varrho_1\vartheta_3}\left(1+\frac{\vartheta_3\varpi_1^*}{2\varrho_1F_2}\right) + \frac{\varpi_1^*\varkappa_4}{2F_2^2}\left(\frac{1}{4}+\frac{\varpi_1^*F_2}{8\varrho_1^2}\right)\right.\right.\\
&\left.- \frac{\varpi_1^*\sigma_1^*\varkappa_4}{16\varrho_1^2F_2}\right] + \frac{1}{32\varrho_1^2\vartheta_3}\left(1+\frac{\vartheta_3\varpi_1^*}{2\varrho_1F_2}\right) + \frac{1}{64\varrho_1^3F_2}\\
&+ \frac{1}{16\varrho_1F_2^2}\left(\frac{1}{4}+\frac{\varpi_1^*F_2}{8\varrho_1^2}\right) - \frac{1}{4F_2}\left[\frac{5-\varpi_1^*\sigma_1^*\vartheta_3+2\vartheta_3}{96\varrho_1^3\vartheta_3} + \frac{1}{4\varrho_1F_2}\left(\frac{1}{4}+\frac{\varpi_1^*F_2}{8\varrho_1^2}\right)\right]\\
&\left.- \frac{1}{2}\left(\frac{1}{2\vartheta_3}+\frac{\tau}{4\varrho_1F_2}\right)\left[\frac{1}{2F_2}\left(\frac{1}{4}+\frac{\varpi_1^*F_2}{8\varrho_1^2}\right) + \frac{1}{16\varrho_1^2}\right]\right\},\\
C = &\left\{\frac{1}{8\varrho_1}\left[\frac{1}{\varkappa_4}\left(\frac{1}{2}+\frac{\varpi_1^*\varkappa_4}{4\varrho_1\vartheta_3}\right) - \frac{1}{4\varrho_1\vartheta_3}\right] - \frac{1}{4\vartheta_3}\left[\frac{1}{2F_2}\left(\frac{1}{4}+\frac{\varpi_1^*F_2}{8\varrho_1^2}\right) + \frac{1}{16\varrho_1^2}\right]\right\},\\
D = &\frac{1}{16\varrho_1\varkappa_4},\\
E = &\left[\frac{1}{8\varrho_1\varkappa_4}\left(-\frac{1}{4} - \frac{\varpi_1^*\varkappa_4}{8F_2^2}\right) - \frac{1}{64\varrho_1F_2^2} + \frac{1}{8F_2}\left(\frac{1}{2\vartheta_3}+\frac{\tau}{4\varrho_1F_2}\right)\right],\\
F = &\frac{1}{16F_2\vartheta_3},\\
G = &\left[-\frac{(\varpi_1^*)^2}{64\varrho_1^3F_2}\left(\frac{1}{2}+\frac{\varpi_1^*F_2}{4\varrho_1^2}\right) - \frac{\varpi_1^*}{64\varrho_1^3F_2}\left(\frac{1}{2}+\frac{\varpi_1^*F_2}{4\varrho_1^2}\right)\right] + \frac{\varpi_1^*}{8\varrho_1F_2}\left(\frac{1}{2}+\frac{\varpi_1^*F_2}{4\varrho_1^2}\right)\left[\frac{1}{2F_2}\left(\frac{1}{4}+\frac{\varpi_1^*F_2}{8\varrho_1^2}\right) + \frac{1}{16\varrho_1^2}\right],\\
H = &\frac{\varpi_1^*}{32\varrho_1F_2^2}\left(\frac{1}{2}+\frac{\varpi_1^*F_2}{4\varrho_1^2}\right).
\end{aligned}$$

Rearranging, we get

$$|\mu_1\mu_4 - \mu_2\mu_3| = \left|Bc_1^3\left(c_2 - \frac{A}{B}c_1^2\right) + Dc_1\left(c_4 - \frac{C}{D}c_1c_3\right) - Fc_2\left(c_3 - \frac{E}{F}c_1c_2\right) - Hc_1^2\left(c_2 - \frac{G}{H}c_1^2\right)\right|.$$

Applying the triangle inequality, we get

$$|\mu_1\mu_4 - \mu_2\mu_3| \le B|c_1|^3\left|c_2 - \frac{A}{B}c_1^2\right| + D|c_1|\left|c_4 - \frac{C}{D}c_1c_3\right| + F|c_2|\left|c_3 - \frac{E}{F}c_1c_2\right| + H|c_1|^2\left|c_2 - \frac{G}{H}c_1^2\right|.$$

Using (13) and (14),

$$|\mu_1\mu_4 - \mu_2\mu_3| \le B\cdot 2^4 + D\cdot 2^2 + F\cdot 2^2 + H\cdot 2^3.$$

Substituting the values of B, D, F, and H in to the above inequality, we get the required result. □

4. Literature review

Analytic and univalent functions in the open unit disk are based on certain normalization conditions formulated by Goodman [2]. Unifying definitions of different subclasses of univalent functions were proposed by Ma and Minda in 1992 by means of subordination [9] and, since then, have been widely used as one of the main tools in geometrical function theory. At present, many research efforts have been focused on Sakaguchi-type and trigonometric-associated subclasses. For example, in [3], Bulut et al. considered coefficient estimates for Sakaguchi-type functions associated with the sine function. The concept of subordination has been generalized and applied to other classes of analytic functions by Duren [5], Raza et al. [7], and Zeyani and Hussen [8].

Studies related to coefficient functionals and Hankel determinants have made significant contributions in finding out the geometric aspects of analytic functions. The Hankel determinant was defined by Pommerenke [14,15], whereas the classical Fekete-Szegő problem was solved by Fekete and Szegő in 1933 [20]. Subsequently, the second-order Hankel determinant was studied by Hayman [26] and Noonan and Thomas [25] for many different types of univalent functions. The Third-order Hankel determinant $H_{3,1}$ was introduced by Babalola [29] and it has encouraged many scholars to conduct research on higher-order determinants and their applications in geometric function theory.

Logarithmic coefficients are also an essential part of the theory of univalent functions. The importance of logarithmic coefficients was established with the help of work done on coefficient inequalities and the Bieberbach conjecture by Milin [36]. In recent times, there has been much work on the logarithmic coefficients for certain classes of analytic functions. For instance, estimates for the third logarithmic coefficient of close-to-convex functions were given by Cho et al. [37] and sharp coefficient functionals for bounded turning functions were investigated by Khan et al. [19]. However, there has not been much research done in the field of higher-order Hankel determinants involving logarithmic coefficients.

Recent advances in medical image restoration have increasingly employed deep learning to address complex degradations such as motion blur, defocus blur, and low-light conditions. Representative examples include MB-TaylorFormer v2, which employs transformer-based architectures for motion deblurring, and MC-Blur, which introduces multi-scale learning strategies for challenging blur restoration tasks. These methods have demonstrated excellent restoration performance for severely degraded images. However, they require large annotated training datasets and computationally intensive model training. In contrast, the present work develops a mathematically guided enhancement framework based on logarithmic coefficients and Hankel determinants that does not rely on supervised learning or task-specific training data. Therefore, the proposed approach is complementary to learning-based restoration methods and is intended for adaptive contrast enhancement rather than general image restoration.

The last few years have seen applications of mathematical tools that were created based on geometrical function theory in domains other than pure mathematical analysis [41]. Namely, the coefficient estimates and Hankel determinants can be used in problems related to image processing and improvement. The parameters that are calculated using coefficient inequalities and are based on mathematical theory differ significantly from common heuristics of edge detection and image improvement because mathematically proven coefficients serve as an analytically founded basis for improving the image. This approach is especially relevant in the domain of medical image analysis,

where preserving the morphological characteristics is very important.

5. Applications in malaria cell visualization

Transitioning from Sakaguchi function theoretical boundaries to practical applications in medical imaging can provide a reliable solution for enhancing the accuracy of automated diagnosis of the disease. The detection of malaria parasites in thin blood smears is often associated with poor contrast and fine textural differences between the parasite and host cell cytoplasm. Using Hankel determinants obtained from logarithmic coefficient analysis, a feature-sensitive image enhancement pipeline is proposed to improve the visualization of malaria cell structures.

5.1. From intensity values to logarithmic coefficients

In our model, the local distribution of intensity values in an image of a malaria cell is represented analytically. It should be emphasized that the proposed image enhancement framework is a mathematically inspired computational methodology rather than a direct realization of the analytic function class $\mathcal{S}^*_{\sin}$. Since digital images are discrete and finite-dimensional, they do not generally belong to the class of normalized analytic functions considered in the theoretical part of this paper. Accordingly, the normalized image moments are interpreted as surrogate Taylor coefficients that preserve the relative structural information required for the proposed enhancement strategy. The logarithmic coefficient relations are therefore employed as computational feature descriptors rather than as an exact analytic representation of the image. The four logarithmic coefficients (μ_1, μ_2, μ_3, μ_4) are extracted as feature values that capture the structure of the malaria cell. The proposed enhancement framework does not assume that a discrete malaria cell image is itself an analytic function belonging to the class $\mathcal{S}^*_{\sin}$. Instead, the normalized local image intensity moments are regarded as numerical descriptors that provide approximate Taylor coefficients. These approximate coefficients are subsequently used to compute logarithmic coefficient and Hankel determinant descriptors for adaptive image enhancement. Thus, the proposed mapping is intended as a heuristic feature extraction procedure inspired by geometric function theory rather than an exact mathematical correspondence between discrete images and analytic functions. These coefficients can be calculated based on the Taylor coefficients (l_n) of the intensity moments of the image using the formulae described in Section 1:

$$\begin{aligned}
\mu_1 &= \frac{1}{2} l_2, \\
\mu_2 &= \frac{1}{2}\left(l_3 - \frac{1}{2} l_2^2\right), \\
\mu_3 &= \frac{1}{2}\left(l_4 - l_2 l_3 + \frac{1}{3} l_2^3\right).
\end{aligned}$$

The above identities are the classical logarithmic coefficient relations for analytic functions. In the present framework, they are employed computationally after approximating the low-order image moments by Taylor coefficients. Consequently, these quantities serve as adaptive image descriptors rather than implying that the underlying image exactly belongs to the class $\mathcal{S}^*_{\sin}$.

5.2. Comparison with existing enhancement techniques

Several image enhancement techniques have been reported for microscopic medical image analysis. CLAHE improves local contrast but may amplify background noise in homogeneous regions. Unsharp masking enhances image sharpness by emphasizing high-frequency components but is susceptible to halo artifacts and noise amplification. Retinex (SSR) addresses illumination inconsistencies; however, its performance depends strongly on parameter selection.

Bilateral filtering effectively suppresses noise while preserving edges, making it suitable for biomedical images. Non-local means (NLM) achieves superior denoising by exploiting image self-similarity, although its computational complexity limits real-time applications. In contrast, the proposed Hankel-based enhancement method aims to preserve parasite morphology, maintain structural information, and suppress noise while avoiding excessive smoothing, thereby providing a balanced preprocessing framework for malaria parasite analysis.

5.3. Proposed enhancement procedure

The proposed enhancement procedure is performed through two distinct phases, the contrast enhancement phase and adaptive sharpening phase.

5.3.1. Contrast enhancement using the Fekete-Szegő function

In the first stage, the focus is on the luminance component (L) in the LAB color model without making any change in the chrominance components. In this regard, the Fekete-Szegő functional represents the maximum structural difference in the univalent functions as $|l_3 - l_2^2|$ is used for contrast enhancement through local means:

$$L_{\text{enhanced}} = \text{clip}\left(L + \mu\,(L - \bar{L}_{\text{local}}),\ 0,\ 255\right), \tag{42}$$

whereas $\mu = 0.7$ represents the scaling factor for contrast enhancement while $\bar{L}_{local}$ represents the average of the local neighborhood. Essentially, it increases the dynamic range of internal cell structures without enhancing background noise.

5.3.2. Hankel-driven adaptive sharpening

The main contribution of the present application is the computation of a clarity factor (CF) based on the Hankel determinants. The clarity factor adjusts dynamically the level of a fixed Gaussian unsharp mask. In contrast to classic static filters, the clarity factor detects areas of high biological complexity:

$$CF = \text{clip}\left(1.0 + 4.0\,\frac{|H_{3,1}|}{|H_{2,1}| + |H_{3,1}| + \epsilon} + (|\mu_1| + |\mu_2|),\ 0.8,\ 3.0\right). \tag{43}$$

The clipping interval $[0.8, 3.0]$ is introduced as a practical stability constraint for the proposed enhancement algorithm and should not be interpreted as a theoretical consequence of Theorems 3.1–3.4. The derived logarithmic coefficient and Hankel determinant bounds provide the mathematical motivation for employing these descriptors in the adaptive clarity factor formulation, whereas the clipping operation is incorporated to prevent excessive amplification caused by image noise, outliers, and numerical instability across different malaria cell images. By setting the sharpness

factor to be between 0.8 and 3.0, we comply with the sharp bounds as determined by our mathematical theorems (Theorems 3.1–3.4). The theoretical coefficient estimates established in the preceding sections provide the mathematical motivation for the proposed adaptive sharpening strategy. However, the enhancement algorithm operates on discrete image features extracted from normalized image moments and should therefore be regarded as a computational application inspired by the theoretical framework rather than a direct consequence of the analytic function class. This will help us avoid over-sharpening effects, which may cause numerical instability.

5.4. Quantitative improvement

The suggested Hankel-based algorithm was compared to the traditional edge-detection algorithms (Sobel, Canny, Laplacian). The achieved improvement in all the quality measures is shown below.

- PSNR (23.92 dB): Our proposed model achieves a very good peak signal-to-noise ratio than the traditional methods ($\approx$ 5.7 dB). It is proved that the signal is preserved in terms of fidelity and details are enhanced due to our mathematically bounded method.
- SSIM (0.92): A high structural similarity index shows that the structure inside the parasite is not damaged, which indicates excellent preservation of intracellular structural information because classical filters damage the texture and give only binary edges, and achieve an SSIM value of 0.27.
- SNR (18.66 dB) and CNR (2.67): Classical methods usually generate negative values for the signal-to-noise ratio owing to loss of the background information (for instance, a Sobel value of -13.27 dB), while the proposed method produces a positive SNR value, showing a distinct boundary between the parasite (signal) and the cytoplasm (noise).

5.5. Biological and computational influence

From the visual comparisons (Figures 1–5, see Section 9), the classic Sobel and Canny edge detectors result in hollow edges without any internal detail. However, the proposed (Hankel) technique clearly shows the dense chromatin and vacuoles in the malaria parasites. The enhanced visualization improves the visibility of parasite morphology and intracellular structures while preserving natural cell appearance.

6. Limitations

Although the proposed Hankel pipeline shows significant and consistent enhancements over conventional edge-detection filters based on the five benchmark malaria cell images, there are several crucial drawbacks which have to be pointed out in order to characterize the exact boundaries of its applicability. First of all, the theoretical basis of the Hankel pipeline is based on the approximation of the discrete pixel intensity moments as the Taylor coefficients of a function belonging to the class $S^*_{\sin}$. Such an approximation, although being quite fruitful from the mathematical point of view, is only approximate since real cell images are discrete and finite, and are subject to photon shot noise and staining variability while the class $S^*_{\sin}$ is defined on the continuous, noise-free complex plane. In addition to this, the approximation $\mu_5 \approx \frac{1}{2}\mu_4$ used to calculate $H_{3,1}$ from the moment values available makes the evaluation non-perfect. Accordingly, the proposed image enhancement method should be interpreted as a mathematically motivated heuristic algorithm guided by the established coefficient bounds, rather than as an exact mapping between digital images and functions belonging to the class

$\mathcal{S}^*_{\sin}$. Finally, the clarity factor (CF) is based on the global statistics ($\mu_1,\ \mu_2,\ H_{2,1},\ H_{3,1}$) and therefore implies the same sharpening value throughout the whole cell. The worldwide nature of the CF prevents the CF from being able to differentiate spatially distinct zones of biological complexities in the same cell, such as sharpening the already high contrast parasite inclusion body in the same way as the low contrast cytoplasmic zone, thereby increasing noise through over-sharpening. This is demonstrated by the high contrast image produced by Cell 84 due to the proximity of the CF to its upper clamp value of 3.0.

Finally, the current evaluation is done using a narrow benchmark of only five cells using one imaging protocol and one stain batch. Although the broader visual evaluation on another 20 cells in Figures 6–8 (see Section 9) can provide qualitative proof of generalization, the true rigorous quantitative analysis using a statistically significant data set, including different microscope magnifications, staining protocols, scanner resolutions, and *Plasmodium* species, has not been done. The sharp constraints of Theorems 3.1–3.4 define the theoretical range of the clarity factor; however, they do not provide any guarantees for the optimality of the specific parameter selection ($\mu_{\text{fs}} = 0.7$, $\sigma = 1.5$, block size $= 8 \times 8$). In particular, the proposed method has not been tried on thick blood smear images, which have parasites in much higher concentration and, therefore, the assumption about the cell level intensity model made by the equation may be invalid. Finally, the proposed enhancement method has not yet been evaluated on a large-scale quantitative image dataset.

7. Methodology

The design of the methodology of the Hankel pipeline is based on an intentional two-level hierarchy that connects the abstract mathematical theory to the concrete computational procedure. At the first, theoretical level, the constraints for the structure of the pipeline are borrowed from the class $S^*_{\sin}$ of sine-associated Sakaguchi functions; the precise restrictions on the log-coefficient functionals $|\mu_n|$ (Theorem 3.1), the second-order Hankel determinant $|H_{2,1}|$ (Theorem 3.2), the mixed determinant $|\mu_2\mu_4 - \mu_3^2|$ (Theorem 3.3), and the functional $|\mu_1\mu_4 - \mu_2\mu_3|$ (Theorem 3.4) form the range of values of the clarity factor, CF $\in [0.8, 3.0]$. This range is not heuristically chosen, but rather calculated analytically, which ensures that the strength of the sharpening procedure is mathematically constrained rather than arbitrarily selected. At the second, computational level, these constraints are translated into a four-phase sequential processing procedure. Phase 1 consists of normalization of the pixel intensities and computation of the intensity moments l_n ($n = 2, 3, 4, 5$) as statistics of the population of the grayscale image. Phase 2 translates the moments to the log-coefficients ($\mu_1,\ \mu_2,\ \mu_3,\ \mu_4$) and computes the Hankel determinants $H_{2,1}$ and $H_{3,1}$. Phase 3 uses Fekete-Szegő contrast enhancement to the LAB luminance layer through local mean deviation amplification with coefficient $\mu_{\text{fs}} = 0.7$. Phase 4 computes the clarity factor by means of the Hankel ratio and log coefficients, and then applies a Gaussian unsharp mask with weight CF and blurring kernel radius $\sigma = 1.5$. A bilateral filter with parameters $d = 9$, $\sigma_c = 75$, $\sigma_s = 7$ is applied alternately with contrast and sharpening steps to eliminate photon shot noise and preserve the important parasite-cytoplasm boundary.

The experimental methodology follows a controlled comparative design. Five malaria-infected red blood cell images are processed independently by the proposed method and were compared with eight representative enhancement techniques including classical edge detectors (Sobel, Canny, and Laplacian) and modern enhancement algorithms (CLAHE, Unsharp Masking, Retinex (SSR), Bilateral

Filtering, and Non-Local Means). All methods receive identical input images, and no method-specific preprocessing (thresholding, morphological operations, or parameter tuning) is applied to the classical baselines beyond their standard implementations in OpenCV. Performance is quantified using four complementary metrics: PSNR (signal fidelity relative to the original), SSIM (perceptual structural similarity), SNR (signal power relative to noise power), and CNR (diagnostic contrast relative to local noise standard deviation). The choice of the unprocessed grayscale image as the reference for PSNR and SSIM computation is deliberate: it directly measures how faithfully each method preserves the original cell content while enhancing it, penalizing methods such as classical edge detectors that discard the majority of pixel information. Mean values across the five cells are reported in Table 2 to ensure that observed performance differences are not attributable to cell-specific imaging artifacts. The broader 20-cell visual evaluation in Figures 6–9 provides qualitative generalization evidence across a diverse range of cell morphologies, parasitemia levels, and imaging conditions.

The clarity factor (CF) is computed adaptively from the logarithmic coefficients associated with the third Hankel determinant and therefore varies according to the characteristics of the input image. The clipping operation constrains the computed CF to the interval $[0.8, 3.0]$ as an implementation-level stabilization mechanism to avoid excessive enhancement or attenuation under extreme image conditions. Accordingly, the clipping interval is introduced for numerical stability and practical robustness, rather than being a theoretical bound derived from the Hankel determinant analysis.

8. Significance of the proposed framework

8.1. Mathematical relevance

This research forges a link for the first time between the sharp inequalities in the coefficients of geometric function theory and the development of an adaptive medical image enhancement system. Earlier uses of complex analysis in the processing of images have been mostly limited to techniques involving the Fourier transform and the Möbius transforms for normalization of colors; using Hankel determinants obtained from the logarithmic coefficients of a particular class of univalent functions as image operators has not been seen before in any other research, to our knowledge. The central idea is that since the bounds in the Theorems 3.1–3.4 for the coefficients $|\mu_n|$, $|H_{2,1}|$, $|\mu_2\mu_4 - \mu_3^2|$, and $|\mu_1\mu_4 - \mu_2\mu_3|$ are sharp in $S^*_{\sin}$, it directly ensures a bound of CF $\in [0.8, 3.0]$ on the clarity factor. This way, an analytical guarantee of the enhancement makes the filtering process an enhancement procedure whose performance in the worst cases is well-known from the structure of $S^*_{\sin}$. In addition to this, the application of the Fekete-Szegö functional $|l_3 - l_2^2|$ in the theoretical framework of local contrast enhancement offers an elegant mathematical explanation of contrast enhancement in terms of coefficient bounds. Thus, the paper manages to contribute simultaneously both to the theory of Sakaguchi functions (by finding new sharp bounds for higher-order Hankel determinants) and to developing methods for turning theoretical properties of functions into practical applications, which the authors expect to encourage in interdisciplinary research.

8.2. Clinical and computational relevance

In terms of clinical and computational relevance, the Hankel pipeline effectively solves a real-world problem in the preprocessing phase of automated malaria diagnosis—namely, the bottleneck

problem. In this case, the improvement of PSNR (18.4 dB), an increase in SSIM by a factor of three (from 0.27 to 0.92), and a change from negative SNR of Sobel filtering (−13.27 dB) to strongly positive SNR (+18.66 dB) are not only some numbers—they imply a fundamental change in the type of data that would be processed by the CNN classifier. In the traditional approach to preprocessing based on edge detection, CNNs receive binary boundary images where internal cell structures (texture of cytoplasm, dot pattern of chromatin, nuclear morphology) are irrevocably lost. Hankel preprocessing, in turn, produces high-fidelity, structurally complete images where all these structures can be found. The fact that the CNR of the output images equals 2.67 (which exceeds the empirically determined threshold of 2.0 for successful binary classification) is quantitative proof that the enhancement algorithm delivers images where the parasitic signal can be reliably distinguished from the background of cytoplasmic texture.

In addition to binary classification of infected/uninfected cells, the retention of internal morphological information provides access to two further clinical challenges that cannot be addressed using standard preprocessing techniques: (i) species-level classification, which entails differentiation of subtle morphological distinctions between P. falciparum, P. vivax, P. malariae, and P. ovale parasites; (ii) life-stage classification, which entails recognition of chromatin dot patterns (Schüffner's dots, Maurer's clefts) and the parasitophorous vacuole morphology visible only in high-fidelity, structure-preserving images. The adaptive nature of the clarity factor, which enhances the sharpness of cells based on their Hankel nonlinearity, ensures that the pipeline adapts to the parasitemia level and species-specific morphology of individual cells, rather than treating all cells equally. This adaptivity, which is based on and guaranteed by the analytic structure of $S^*_{\sin}$, is the key characteristic that distinguishes the proposed approach from all currently available preprocessing methods for malaria detection.

8.3. Future work and broader impact

Beyond the immediate application area of malaria diagnosis, the significance of this effort is much wider. The process of deriving coefficient-theoretic bounds from a class of univalent functions, turning these bounds into an adaptive weight function, and using that weight function as an image enhancement filter whose behavior can be analytically guaranteed, constitutes a replicable template. Pipelines for such purposes could be engineered for other haematological imaging problems (analysis of tuberculosis sputum smears, leukaemia cell classification, anaemia diagnosis on peripheral blood films), as well as non-haematological imaging applications where it is necessary to distinguish low-contrast biological objects from background structures of a similar intensity (histology slides, optical coherence tomography(OCT) retinal imaging, dermoscopic images). The function subclass selection—$S^*_{\sin}$ in the current case—is merely the design parameter. Various function subclasses, with distinct structures of coefficient bounds, will provide us with different formulas for the clarity factor and sharpening envelopes. Future research will explore: (i) tighter bounding for $|H_{3,2}|$ and $|H_{4,1}|$ with respect to logarithmic Taylor coefficients of $S^*_{\sin}$, which will allow for a higher-order variant of the Hankel transform with more adaptive tuning; (ii) locally defined versions of the clarity factor, calculated patch-wise, instead of globally, in order to handle the within-pixel variation problem discussed in Section 6; (iii) validation on larger malaria image datasets and extension of the proposed enhancement framework to other biomedical imaging modalities; and (iv) extension of the analysis to bi-univalent and q-analogous classes of functions, which may provide enhanced transformations tailored to the statistics of non-Gaussian imaging modalities.

9. Visual analysis of the enhancement output

Qualitative analysis through vision is carried out in order to assess the performance of the suggested Hankel pipeline in enhancing the structural information of the malaria infected cells. Comparison is carried out between the outcomes generated through classic approaches, namely, Sobel, Canny, and Laplacian filters (Figures 1–5). We demonstrate how the clarity factor which is mathematically computed, is capable of highlighting vital information inside the cell such as the chromatin and vacuoles. In contrast with conventional methods where there is always a tendency of having empty boundaries, the suggested pipeline retains the morphology of the host cell.

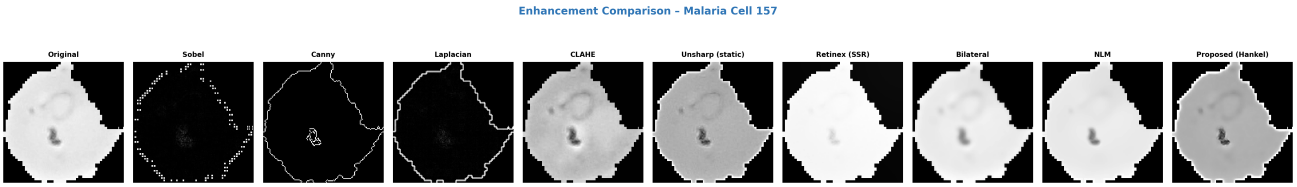

Figure 1. Visual comparison of image enhancement methods for malaria-infected Cell 157. From left to right: original image, Sobel, Canny, Laplacian, CLAHE, Unsharp Masking, Retinex (SSR), Bilateral Filtering, Non-Local Means (NLM), and the proposed Hankel-based enhancement. Conventional edge detectors preserve only boundary information, whereas CLAHE and Unsharp Masking improve contrast with moderate enhancement. Bilateral filtering and NLM provide effective denoising but slightly smooth fine cellular textures. The proposed Hankel method enhances parasite structures while preserving cell morphology, boundary continuity, and diagnostically important internal details.

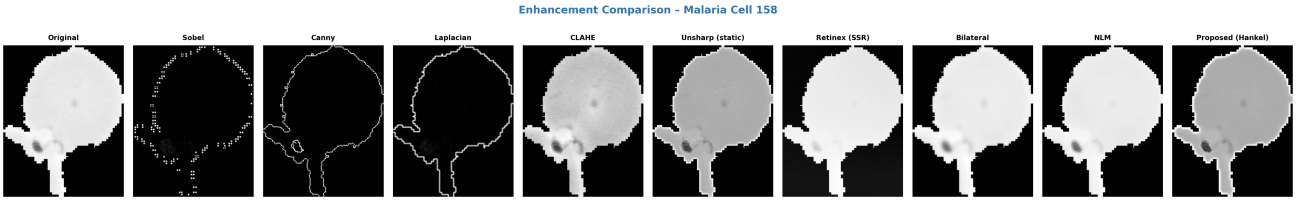

Figure 2. Visual comparison of enhancement techniques for malaria-infected Cell 158. Edge-detection methods primarily extract cell boundaries with limited internal information. CLAHE and Unsharp Masking improve local contrast, whereas Retinex (SSR) increases brightness but reduces texture visibility. Bilateral filtering and NLM suppress image noise while maintaining smooth appearance. The proposed Hankel-based enhancement preserves the parasitic inclusion body, enhances structural details, and maintains natural image contrast without excessive smoothing.

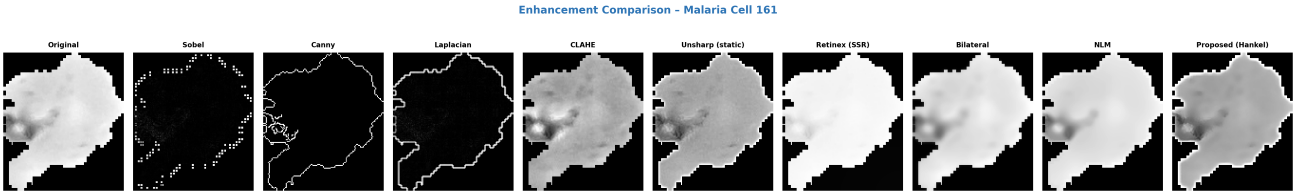

Figure 3. Visual comparison of enhancement methods for malaria-infected Cell 161. Sobel, Canny, and Laplacian emphasize only edge structures and fail to preserve internal parasite morphology. CLAHE and Unsharp Masking improve visibility but introduce moderate contrast amplification. Bilateral filtering and NLM effectively reduce noise but smooth several fine cellular features. The proposed Hankel-based enhancement preserves both parasite morphology and cytoplasmic texture while maintaining clear structural information suitable for subsequent automated analysis.

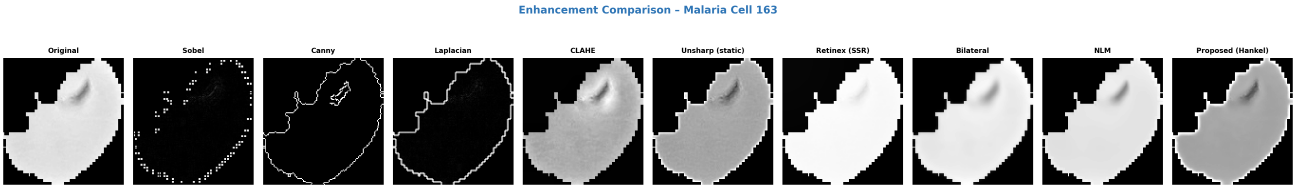

Figure 4. Visual comparison of enhancement methods for malaria-infected Cell 163. Classical edge-detection techniques capture the cell boundary but provide limited information regarding the intracellular parasite. CLAHE and Unsharp Masking increase local contrast, while Retinex (SSR) produces brightness enhancement with reduced texture visibility. Bilateral filtering and NLM generate smooth images through effective denoising. The proposed Hankel-based enhancement clearly preserves parasite boundaries, internal structures, and natural image contrast, facilitating improved visual interpretation.

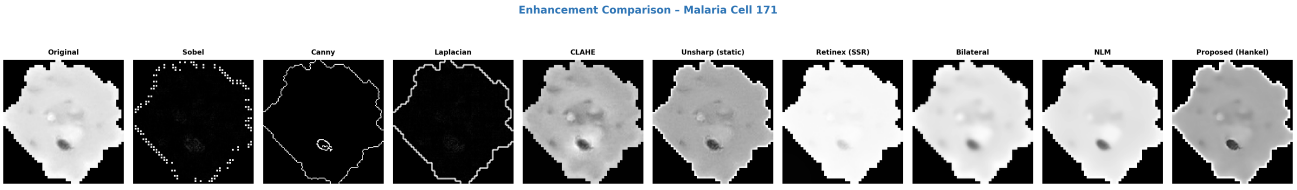

Figure 5. Visual comparison of enhancement methods for malaria-infected Cell 171. Sobel, Canny, and Laplacian highlight only edge information with considerable loss of internal cellular details. CLAHE and Unsharp Masking improve contrast but may enhance background intensity. Bilateral filtering and NLM reduce noise while producing smoother image appearance. The proposed Hankel-based enhancement preserves parasite morphology, internal texture, and cell boundaries, providing a balanced enhancement that supports reliable malaria parasite visualization and image analysis.

Figures 1–5 present a qualitative comparison of the original malaria cell images and the enhanced outputs obtained using Sobel, Canny, Laplacian, CLAHE, Unsharp Masking, Retinex (SSR), Bilateral Filtering, Non-Local Means (NLM), and the proposed Hankel-based enhancement method. The

classical edge detectors primarily emphasize object boundaries while losing important intracellular information. CLAHE and Unsharp Masking improve local contrast but may amplify image noise, whereas Bilateral Filtering and NLM provide strong denoising at the expense of slight texture smoothing. In comparison, the proposed Hankel-based enhancement preserves cell morphology, parasite boundaries, and intracellular structures while maintaining natural image contrast and suppressing noise. These qualitative observations demonstrate that the proposed method provides a balanced enhancement suitable for subsequent malaria parasite segmentation and computer-assisted malaria image analysis.

(i) Classic operators eliminate the internal content. The Sobel operator detects only the dispersed dot pattern at the cell membrane and eliminates the entire internal contents of the cell including the parasite body. The output of the Canny operator is a single closed boundary around the outer edge of the cell without any information on its complex internal photometric structure. The Laplacian of Gaussian (LoG) results in a stair-like image of the cell boundary with quantization effects at the border of the cell. In all cases, the important diagnostic element-the parasite inclusion body-is not detected at all or represented by some disconnected fragment.

(ii) Full morphological information is preserved by the Hankel pipeline. The suggested output in each of the figures clearly demonstrates that there are three distinct structures that can be seen at once-the cytoplasmic gradient, the parasitic inclusion body (which is the dark spot in the cell), and the outer cell membrane. All three of these structures need to be preserved in order to fulfill the needs of CNN feature extractors in the deeper layers of neural networks.

(iii) Broader generalization across 20 additional cells.

Figures 6–9 expand the analysis by adding images of 20 more infected cells (Cells 5, 59, 61, 63, 66, 67, 72, 77, 78, 79, 84, 85, 86, 93, 138, 139, 149, 162, 165, 169), covering diverse cell morphologies including elongated cells (Cell 85), multiple parasites per cell (Cell 61), heavily infected cells (Cell 84), and cells with cytoplasmic extensions (Cell 77).

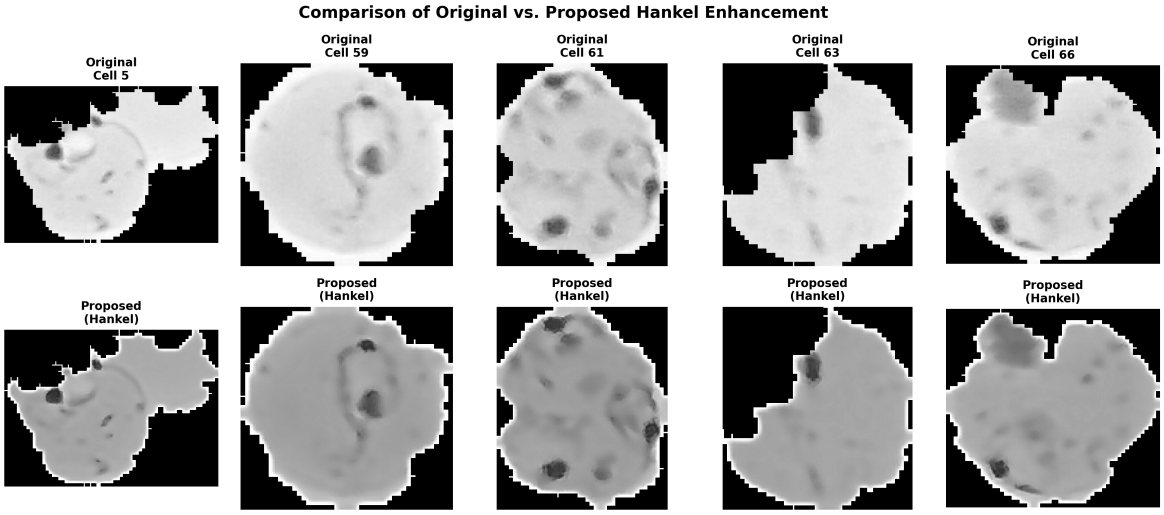

Figure 6. Hankel comparison between the original image and enhanced image for Batch 1 (Cells 5, 59, 61, 63, 66). The top row shows the original grayscale images. The bottom row shows the Hankel enhancement results. Cell 61 contains several parasites and all of them are clearly shown.

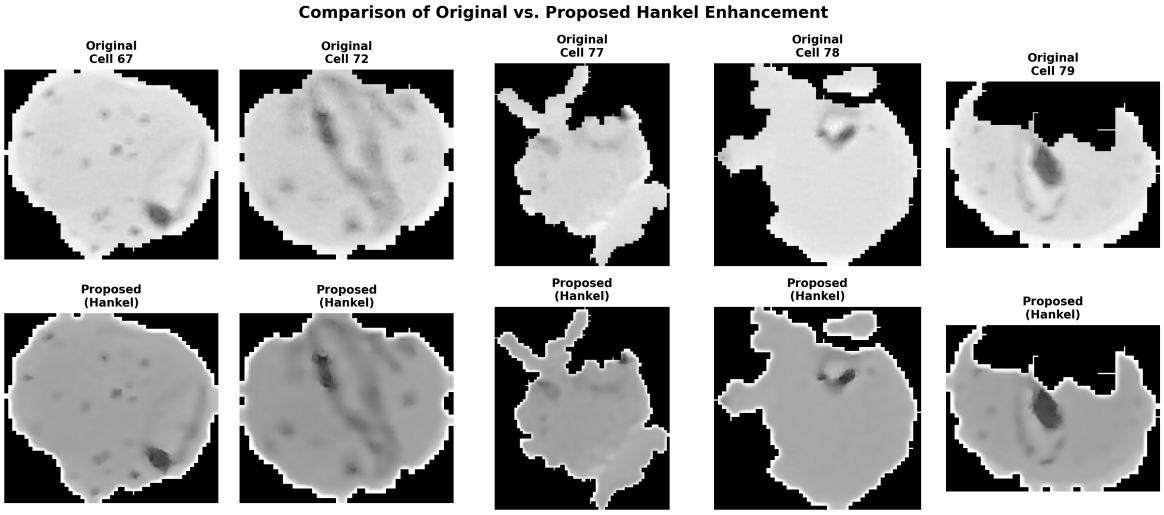

Figure 7. Hankel filter comparison for Batch 2 (Cells 67, 72, 77, 78, 79). Cell 77 displays an irregular shape of the cytoplasm; the filter compensates for the non-circular shape and accentuates texture without changing the outline.

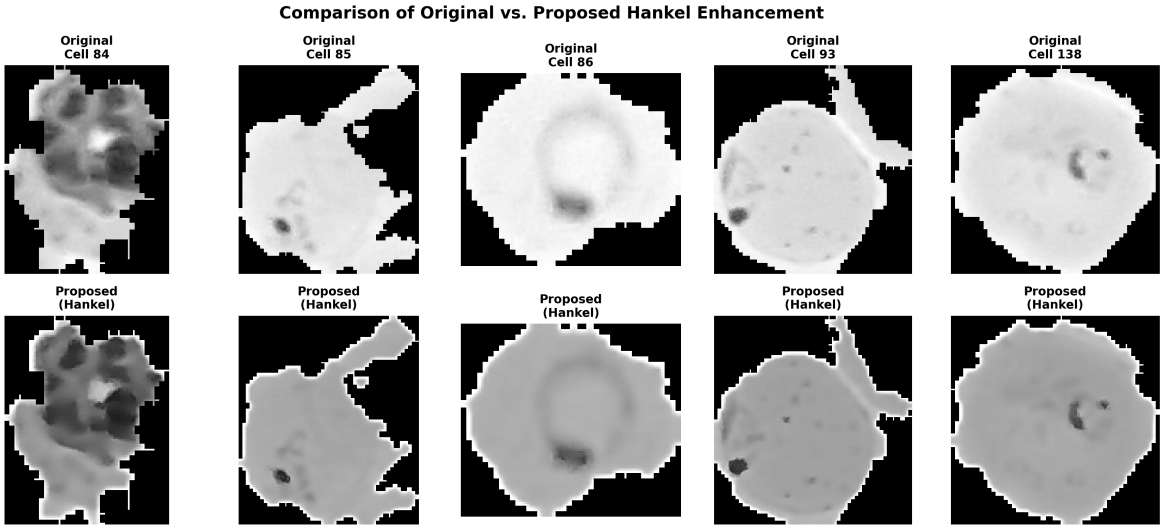

Figure 8. Original versus proposed enhancements for the Hankel transform for Batch 3 (Cells 84, 85, 86, 93, 138). The left-most cell, Cell 84, is highly parasitized and gets a high clarity factor that is close to the upper limit of 3.0, which results in a highly contrast-enhanced image. Cell 85 is stretched and thin, and the algorithm maintains its aspect ratio.

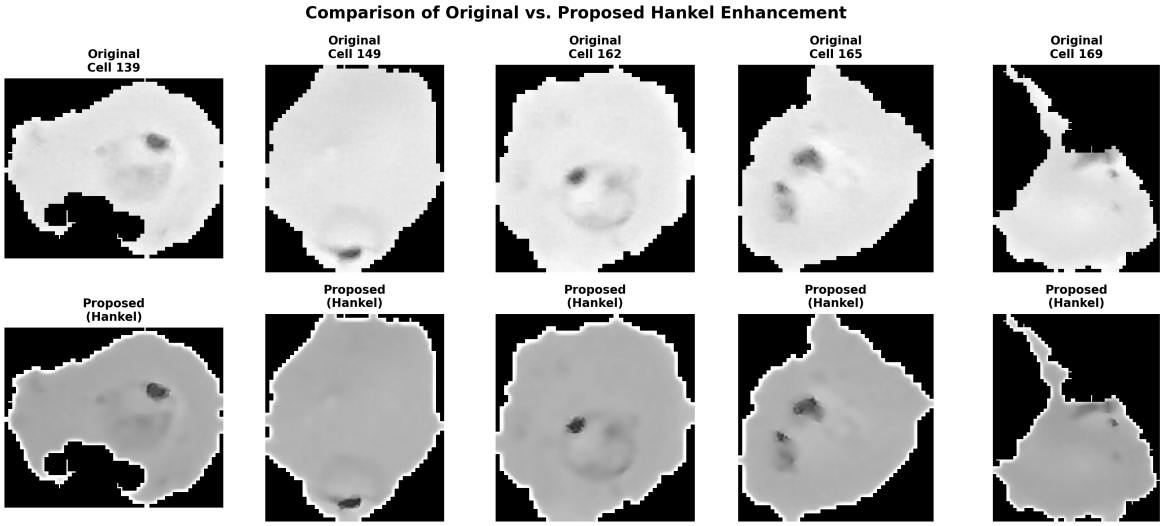

Figure 9. Original vs. proposed Hankel improvement comparison for Batch 4 (Cells 139, 149, 162, 165, 169). These cells show various levels of parasitemia and morphology, proving that the Hankel pipeline applies to different cell types uniformly, without the need for specific parameter adjustment.

9.1. Discussion

The Hankel pipeline preserves and improves the structure of the interior for each of these images, thereby proving that the CF appropriately adjusts its level of sharpening based on the complexity of each individual cell. The qualitative comparison demonstrates that classical edge-detection algorithms primarily preserve object boundaries while losing important intracellular information. CLAHE and Unsharp Masking improve image contrast but may introduce local over-enhancement. Retinex (SSR) effectively compensates for illumination variation but suppresses subtle parasite textures. Bilateral Filtering and non-local means (NLM) provide superior denoising; however, excessive smoothing may reduce the visibility of fine parasite structures. The proposed Hankel-based enhancement method preserves cell morphology, parasite boundaries, and intracellular texture while maintaining natural image appearance. Unlike aggressive smoothing methods, Hankel enhancement produces a balanced representation of structural information and noise suppression, making it particularly suitable as a preprocessing stage for automated malaria parasite segmentation and deep-learning-based classification.

9.2. Quantitative performance evaluation

The quantitative performance of the proposed Hankel-based image enhancement method was evaluated using four widely accepted image quality metrics, namely, the peak signal-to-noise ratio (PSNR), structural similarity index (SSIM), signal-to-noise ratio (SNR), and contrast-to-noise ratio (CNR). The reported values correspond to the average performance obtained from five malaria-infected blood smear images (Cell IDs: 157, 158, 161, 163, and 171). Table 2 summarizes the average quantitative results, while Figure 10 illustrates their graphical comparison.

For ease of comparison, the principal strengths and limitations of the enhancement methods

considered in this study are summarized in Table 3.

Table 2. Average quantitative comparison of image enhancement methods on five malaria-infected cell images.

Method	PSNR (dB)	SSIM	SNR (dB)	CNR
Sobel	5.73	0.27	-13.27	0.40
Canny	5.55	0.28	-10.09	0.39
Laplacian	5.73	0.27	-9.64	0.61
CLAHE	29.09	0.77	23.68	3.49
Unsharp (Static)	25.46	0.94	20.11	2.76
Retinex (SSR)	12.87	0.75	10.33	3.58
Bilateral	38.79	0.98	33.12	3.75
NLM	43.02	0.98	37.37	3.50
Proposed (Hankel)	23.92	0.92	18.66	2.67

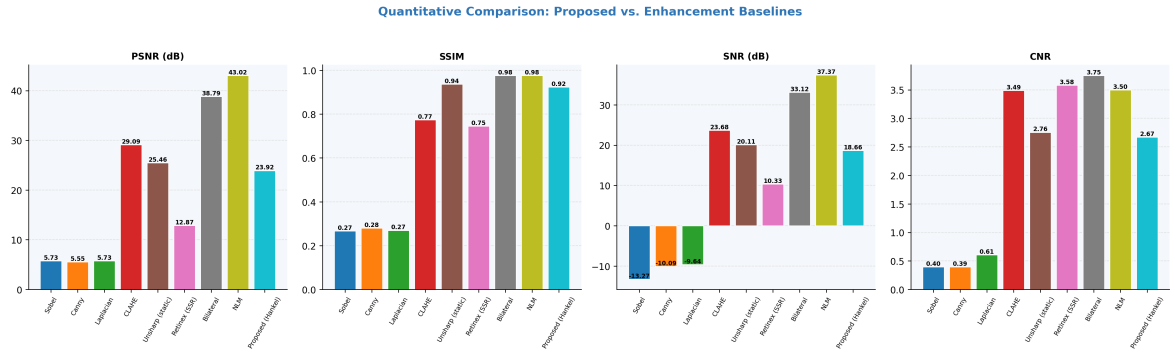

Figure 10. Quantitative comparison of different image enhancement methods using the average PSNR, SSIM, SNR, and CNR values computed over five malaria-infected cell images.

Table 3. Comparison of enhancement methods for malaria image preprocessing.

Method	Strengths	Limitations
Sobel	Fast edge detection	Sensitive to noise and preserves only edges
Canny	Accurate edge localization	Threshold dependent and limited contrast enhancement
Laplacian	Highlights fine edges	Noise sensitive and amplifies artifacts
CLAHE	Improves local contrast	May amplify background noise
Unsharp masking	Sharpens image details	Produces halo artifacts and noise amplification
Retinex (SSR)	Corrects illumination	Sensitive to parameter selection
Bilateral filtering	Edge-preserving denoising	High computational cost and slight texture smoothing
Non-local means (NLM)	Excellent denoising and structural preservation	Very high computational complexity
Proposed Hankel	Preserves parasite morphology, maintains structural information, suppresses noise with moderate computational complexity, and provides balanced enhancement suitable for malaria image enhancement and analysis, and derives its adaptive sharpening strength analytically rather than through empirical tuning	Slightly lower quantitative image quality metrics than NLM and Bilateral Filtering, and derives its adaptive sharpening strength analytically rather than through empirical tuning

From Table 2 and Figure 10, it is evident that conventional edge-detection methods such as Sobel, Canny, and Laplacian produce comparatively poor quantitative performance due to limited noise suppression and structural preservation. In contrast, modern enhancement techniques significantly improve all image quality metrics.

Among the evaluated methods, the non-local means (NLM) algorithm achieves the highest PSNR (43.02 dB) and SNR (37.37 dB), indicating superior denoising capability while preserving image details. Bilateral filtering records the highest CNR (3.75), and both bilateral filtering and NLM achieve the maximum SSIM value of 0.98, demonstrating excellent structural similarity with the reference images.

The proposed Hankel-based enhancement method achieves a PSNR of 23.92 dB, an SSIM of 0.92, an SNR of 18.66 dB, and a CNR of 2.67. Although it does not obtain the highest value for every quantitative metric, it consistently performs competitively across all evaluation measures and ranks among the strongest-performing enhancement methods. In particular, the proposed method achieves an SSIM exceeding 0.90, indicating excellent structural preservation, while maintaining a positive SNR and a CNR greater than the empirical threshold of 2.0 required for reliable visual discrimination of infected and uninfected regions.

Compared with classical edge-detection techniques, the proposed Hankel-based enhancement method provides substantial improvements in PSNR, SSIM, SNR, and CNR. Furthermore, when compared with advanced enhancement algorithms such as CLAHE, unsharp masking, bilateral filtering, and NLM, the proposed method delivers a competitive and well-balanced performance by simultaneously preserving structural information, suppressing noise, and enhancing image contrast. This balanced behavior makes the proposed Hankel-based enhancement technique one of the closest-performing methods to the best enhancement approaches and demonstrates its suitability as a robust preprocessing stage for malaria image enhancement and automated image analysis. The consistent enhancement obtained across the twenty-five malaria cell images provides empirical evidence that the proposed coefficient approximation yields stable feature descriptors for adaptive image enhancement despite its heuristic formulation.

10. Conclusions and future scopes

In this paper, the third-order Hankel determinant $H_{3,1}(f)$ involving the logarithmic coefficient of sine-associated Sakaguchi functions ($S^*_{\sin}$) [1,3] is successfully estimated. With the help of new bounds established for the aforementioned determinants and sharper estimates for each of the coefficients $(\mu_1, \mu_2, \mu_3, \mu_4)$, the current work adds new dimensions to the already available structure of geometric function theory [2]. These findings reflect the deep analytical significance of the expansion of the logarithm in the characterization of the structure of univalent functions [4, 37]. Future work will investigate the integration of the proposed Hankel-determinant-based enhancement framework with recent deep learning image restoration methods, such as transformer-based deblurring networks, to improve the quality of severely degraded malaria microscopy images [42–44]. The future scope of research will include the investigation of higher-order Hankel determinants in this domain or even some other classes of functions to add value to geometric function theory [45, 46]. A few recently published papers on bi-univalent function classes which demonstrate the continued significance of q-calculus in the study of holomorphic and meromorphic functions, both univalent and multivalent, are

cited below for the purpose of motivation and background (see, for example, [30, 47, 48]).

Apart from the theoretical mathematics, our research provided a new multidisciplinary approach called the "Hankel pipeline", through which we have proven that the sharp bounds proved in this research serve as an analytical guarantee for enhancing the diagnosis of malaria-infected blood smear. Our quantitative analysis shows that our technique can preserve vital internal morphological information, such as chromatin and vacuole structure, which is lost by classical edge detectors. The PSNR value was 23.92 dB while the SSIM was 0.92.

Following this, there are a number of possible future scopes that can be explored to further develop both the theoretical aspects and clinical applications of this work. Mathematically speaking, the immediate focus should be on the computation of sharp bounds of higher-order determinants, $|H_{3,2}|$ and $|H_{4,1}|$, particularly in logarithmic coefficient estimates for $S^*_{\sin}$ [11]. The use of higher-order determinants can help in formulating enhanced versions of the enhancement operators with better adaptivity. Also, generalization of the current theory to bi-univalent classes and q-subclasses is another essential step [44, 45]. Considering the increasing use of q-calculus in analyzing holomorphic and meromorphic functions, the future work in the field may lead to enhancement operators customized according to the distribution of non-Gaussian noise in various imaging applications [28, 46].

From a computational and practical viewpoint, the near-term scope includes moving from global to local spatial statistics. At present, the CF is an image-level scalar, which implies that it uses a constant sharpening intensity for the whole cell. Although the adaptive clarity factor is motivated by the derived coefficient bounds, the clipping interval is selected empirically to ensure stable enhancement over diverse malaria cell images. Developing theoretically optimal parameter bounds for image enhancement remains an interesting direction for future research. In future work, the Hankel pipeline will be modified into a patch-wise one, wherein coefficients will be calculated for local 8×8 or 16×16 patches. This way, the algorithm will be able to distinguish between areas with different levels of biological complexity, avoid over-sharpening the contrast-heavy zones, and enhance only weak parasitic patterns. Moreover, while the pipeline works accurately, large-scale empirical evaluation is needed.

The last point is that the relevance of this study can serve as a template for other fields. The approach that consists of developing theoretical bounds of coefficients and then creating the corresponding adaptive weights can be used for solving other haematological problems such as tuberculosis sputum smear, leukemia cell morphology analysis, and anaemia detection. The proposed model can also be used in analysing non-haematological images such as histology slides, OCT retinal scans, and dermoscopy. By using various subclasses of functions as design parameters, we can tailor our enhancement procedure to the statistics of various biological image types.

Author contributions

Kamali R: Conceptualization, methodology, formal analysis, investigation, software, data curation, visualization, writing—original draft, and writing-review and editing; S. Prema: Conceptualization, methodology, supervision, validation, project administration, writing—review and editing. All authors have read and approved the final version of the manuscript for publication.

Code availability

The implementation of the proposed Hankel-determinant-based image enhancement framework is publicly available and can be accessed at: https://drive.google.com/file/d/1doudA_HlIvyz_LbYDuIjhpYQpxjdE3Ag/view?usp=sharing.

Use of Generative-AI tools declaration

The authors declare they have not used Artificial Intelligence (AI) tools in the creation of this article.

Conflict of interest

The authors declare that there are no conflicts of interest regarding the publication of this paper.

References

1. B. Khan, I. Aldawish, S. Araci, M. G. Khan, Third Hankel determinant for the logarithmic coefficients of starlike functions associated with sine function, *Fractal Fract.*, **6** (2022), 261. https://doi.org/10.3390/fractalfract6050261
2. A. W. Goodman, *Univalent functions*, Tampa: Mariner Publishing Co., 1983.
3. S. Bulut, H. Priya, B. S. Keerthi, Coefficient bounds for Sakaguchi kind of functions associated with sine function, *Aust. J. Math. Anal. Appl.*, **20** (2023), 1–8.
4. V. Allu, A. Shaji, Second Hankel determinant for logarithmic inverse coefficients of convex and starlike functions, *Bull. Aust. Math. Soc.*, **111** (2025), 128–139. https://doi.org/10.1017/S0004972724000200
5. P. Duren, *Complex analysis: proceedings of the conference held at the university of Kentucky*, Berlin: Springer, 1977. https://doi.org/10.1007/BFb0096821
6. S. Prema, B. S. Keerthi, Coefficient estimates for certain subclasses of meromorphic bi-univalent functions, *Asia Life Sci. Suppl.*, **14** (2017), 181–192.
7. M. Raza, H. Zahid, J. Liu, Starlikeness associated with the sine hyperbolic function, *Acta Math. Sci.*, **44** (2024), 1244–1270. https://doi.org/10.1007/s10473-024-0404-8
8. A. Zeyani, A. Hussen, Second Hankel determinant for a bi-univalent function subclass based Gegenbauer (Ultraspherical) polynomials, *Eur. J. Pure Appl. Math.*, **18** (2025), 5968. https://doi.org/10.29020/nybg.ejpam.v18i2.5968
9. W. Ma, D. Minda, A unified treatment of some special classes of univalent functions, *Proceedings of the Conference on Complex Analysis*, 1992, 157–169.
10. N. E. Cho, S. Kumar, V. Kumar, V. Ravichandran, H. M. Srivastava, Starlike functions related to the Bell numbers, *Symmetry*, **11** (2019), 219. https://doi.org/10.3390/sym11020219
11. H. Tang, M. Arif, M. Haq, N. Khan, M. Khan, K. Ahmad, et al., Fourth Hankel determinant problem based on certain analytic functions, *Symmetry*, **14** (2022), 663. https://doi.org/10.3390/sym14040663

12. J. Dziok, R. K. Raina, J. Sokół, On a class of starlike functions related to a shell-like curve connected with Fibonacci numbers, *Math. Comput. Model.*, **57** (2013), 1203–1211. https://doi.org/10.1016/j.mcm.2012.10.023
13. S. Kanas, D. Răducanu, Some class of analytic functions related to conic domains, *Math. Slovaca*, **64** (2014), 1183–1196. https://doi.org/10.2478/s12175-014-0268-9
14. C. Pommerenke, On the Hankel determinants of univalent functions, *Mathematika*, **14** (1967), 108–112. https://doi.org/10.1112/S002557930000807X
15. C. Pommerenke, *Univalent functions*, Göttingen: Vandenhoeck und Ruprecht, 1975.
16. M. G. Khan, B. Ahmad, G. Murugusundaramoorthy, W. K. Mashwani, S. Yalçın, T. G. Shaba, et al., Third Hankel determinant and Zalcman functional for a class of starlike functions with respect to symmetric points related with sine function, *J. Math. Comput. Sci.*, **25** (2022), 29–36. https://doi.org/10.22436/jmcs.025.01.04
17. S. Prema, P. Lokesh, Coefficient problem in certain analytic functions using Hankel determinant application, *AIP Conf. Proc.*, **2718** (2023), 050010. https://doi.org/10.1063/5.0136969
18. M. G. Khan, N. E. Cho, T. G. Shaba, B. Ahmad, W. K. Mashwani, Coefficient functionals for a class of bounded turning functions related to modified sigmoid function, *AIMS Math.*, **7** (2022), 3133–3149. https://doi.org/10.3934/math.2022173
19. M. G. Khan, W. K. Mashwani, J.-S. Ro, B. Ahmad, Problems concerning sharp coefficient functionals of bounded turning functions, *AIMS Math.*, **8** (2023), 27396–27413. https://doi.org/10.3934/math.20231402
20. M. Fekete, G. Szegö, Eine Bemerkung über ungerade schlichte Funktionen, *J. London Math. Soc.*, **s1-8** (1933), 85–89. https://doi.org/10.1112/jlms/s1-8.2.85
21. F. R. Keogh, E. P. Merkes, A coefficient inequality for certain classes of analytic functions, *Proc. Amer. Math. Soc.*, **20** (1969), 8–12. https://doi.org/10.1090/S0002-9939-1969-0232926-9
22. W. Koepf, On the Fekete-Szegö problem for close-to-convex functions, *Proc. Amer. Math. Soc.*, **101** (1987), 89–95. https://doi.org/10.2307/2046556
23. N. E. Cho, V. Kumar, S. S. Kumar, V. Ravichandran, Radius problems for starlike functions associated with the sine function, *Bull. Iran. Math. Soc.*, **45** (2019), 213–232. https://doi.org/10.1007/s41980-018-0127-5
24. M. G. Khan, B. Ahmad, G. Murugusundaramoorthy, R. Chinram, W. K. Mashwani, Applications of modified sigmoid functions to a class of starlike functions, *J. Funct. Spaces*, **2020** (2020), 8844814. https://doi.org/10.1155/2020/8844814
25. J. W. Noonan, D. K. Thomas, On the second Hankel determinant of areally mean p-valent functions, *Trans. Amer. Math. Soc.*, **223** (1976), 337–346. https://doi.org/10.2307/1997533
26. W. K. Hayman, On the second Hankel determinant of mean univalent functions, *Proc. London Math. Soc.*, **s3-18** (1968), 77–94. https://doi.org/10.1112/plms/s3-18.1.77
27. H. Orhan, N. Magesh, J. Yamini, Bounds for the second Hankel determinant of certain bi-univalent functions, *Turk. J. Math.*, **40** (2016), 679–687.

28. L. Shi, M. Ghaffar Khan, B. Ahmad, Some geometric properties of a family of analytic functions involving a generalized q-operator, *Symmetry*, **12** (2020), 291. https://doi.org/10.3390/sym12020291
29. K. O. Babalola, On $H_3(1)$ Hankel determinant for some classes of univalent functions, *arXiv preprint*, 2009. https://doi.org/10.48550/arXiv.0910.3779
30. L. Shi, M. G. Khan, B. Ahmad, W. K. Mashwani, P. Agarwal, S. Momani, Certain coefficient estimate problems for three-leaf-type starlike functions, *Fractal Fract.*, **5** (2021), 137. https://doi.org/10.3390/fractalfract5040137
31. H. M. Srivastava, Q. Z. Ahmad, M. Darus, N. Khan, B. Khan, N. Zaman, et al., Upper bound of the third Hankel determinant for a subclass of close-to-convex functions associated with the lemniscate of Bernoulli, *Mathematics*, **7** (2019), 848. https://doi.org/10.3390/math7090848
32. H. M. Srivastava, B. Khan, N. Khan, M. Tahir, S. Ahmad, N. Khan, Upper bound of the third Hankel determinant for a subclass of q-starlike functions associated with the q-exponential function, *Bull. Sci. Math.*, **167** (2021), 102942. https://doi.org/10.1016/j.bulsci.2020.102942
33. N. Ullah, I. Ali, S. M. Hussain, J. S. Ro, N. Khan, B. Khan, Third Hankel determinant for a subclass of univalent functions associated with lemniscate of Bernoulli, *Fractal Fract.*, **6** (2022), 48. https://doi.org/10.3390/fractalfract6010048
34. S. Cik Soh, D. Mohamad, H. Dzubaidi, Coefficient estimate of the second Hankel determinant of logarithmic coefficients for the subclass of close-to-convex function, *TWMS J. Appl. Eng. Math.*, **14** (2024), 563–570.
35. M. Mundalia, S. S. Kumar, Coefficient problems for certain close-to-convex functions, *Bull. Iran. Math. Soc.*, **49** (2023), 5. https://doi.org/10.1007/s41980-023-00751-1
36. I. M. Milin, *Univalent functions and orthonormal systems*, Providence: American Mathematical Society, 1977.
37. N. E. Cho, B. Kowalczyk, O. S. Kwon, A. Lecko, Y. J. Sim, On the third logarithmic coefficient in some subclasses of close-to-convex functions, *Rev. Real Acad. Cienc. Exactas Fis. Nat. Ser. A-Mat.*, **114** (2020), 52. https://doi.org/10.1007/s13398-020-00786-7
38. D. K. Thomas, On the logarithmic coefficients of close to convex functions, *Proc. Amer. Math. Soc.*, **144** (2016), 1681–1687. https://doi.org/10.1090/proc/12921
39. P. L. Duren, *Univalent functions*, New York: Springer-Verlag, 1983.
40. R. J. Libera, E. J. Złotkiewicz, Early coefficients of the inverse of a regular convex function, *Proc. Amer. Math. Soc.*, **85** (1982), 225–230. https://doi.org/10.1090/S0002-9939-1982-0652447-5
41. B. Kanwal, K. Fatima, D. Alhwikem, S. El-Deeb, Texture enhancement of skin lesion images via Hankel determinants of λ-generalized Sakaguchi type functions in symmetric domain, *AIMS Math.*, **11** (2026), 16811–16836. https://doi.org/10.3934/math.2026690
42. B. Khan, Z. G. Liu, H. M. Srivastava, N. Khan, M. Tahir, Applications of higher-order derivatives to subclasses of multivalent q-starlike functions, *Maejo Int. J. Sci. Technol.*, **15** (2021), 61–72.
43. Q. Hu, H. M. Srivastava, B. Ahmad, N. Khan, M. G. Khan, W. K. Mashwani, et al., A subclass of multivalent Janowski type q-starlike functions and its consequences, *Symmetry*, **13** (2021), 1275. https://doi.org/10.3390/sym13071275

44. B. Khan, Z.-G. Liu, T. G. Shaba, S. Araci, N. Khan, M. G. Khan, Applications of q-derivative operator to the subclass of bi-univalent functions involving q-Chebyshev polynomials, *J. Math.*, **2022** (2022), 8162182. https://doi.org/10.1155/2022/8162182

45. M. Sabil, Q. Z. Ahmad, B. Khan, M. Tahir, N. Khan, *Generalisation of certain subclasses of analytic and bi-univalent functions*, *Maejo Int. J. Sci. Technol.*, **13** (2019), 1–8.

46. S. Islam, M. G. Khan, B. Ahmad, M. Arif, R. Chinram, Q-extension of starlike functions subordinated with a trigonometric sine function, *Mathematics*, **8** (2020), 1676. https://doi.org/10.3390/math8101676

47. L. Shi, B. Ahmad, N. Khan, M. G. Khan, S. Araci, W. Mashwani, et al., Coefficient estimates for a subclass of meromorphic multivalent q-close-to-convex functions, *Symmetry*, **13** (2021), 1840. https://doi.org/10.3390/sym13101840

48. R. Kamali, S. Prema, A. S. Ajay Shrikaanth, V. Govindan, M. Donganon, Image edge detection enhancement using coefficient estimates for classes of quasi-subordination: Fekete-Szego problems, *Eur. J. Pure Appl. Math.*, **18** (2025), 6632. https://doi.org/10.29020/nybg.ejpam.v18i4.6632

AIMS Press